TAPPI JOURNAL
WWW.TAPPI.ORG
THE PAPER AND PACKAGING INDUSTRIES' TECHNICAL RESOURCE
JANUARY 2010 | VOL. 9 NO. 1

PAPER OPTICAL PROPERTIES 4
Papermaking potential of novel structured PCC fillers with enhanced refractive index
Kimmo Koivunen and Hannu Paulapuro

COMPUTER SIMULATION 15
Prediction of handsheet tensile strength by computational simulation of structure
Rémi Vincent, Martine Rueff, and Christian Voillot

WASTEWATER TREATMENT 20
Characterizing carbonaceous biochemical oxygen demand load reductions from pulp and paper mills for activities related to total maximum daily loads
James E. Palumbo and Linfield C. Brown

COATING 27
Calendering effects on coating pore structure and ink setting behavior
Peter Resch, Wolfgang Bauer, and Ulrich Hirn

»Todos os títulos no JORNAL de TAPPI estão traduzidos agora em português.

»所有<< 纸浆与纸工业技术协会杂志>>文章标题现在都被译成中文

January 2010

TAPPI JOURNAL
WWW.TAPPI.ORG

TABLE OF CONTENTS VOL. 9 NO. 1

3 EDITORIAL

Moving forward
Monica Shaw

4 PAPER OPTICAL PROPERTIES

Papermaking potential of novel structured PCC fillers with enhanced refractive index

Potencial fabricação de papel de novas cargas de PCC estruturado com avançado índice refrativo

利用具有增强折射率的异常结构的PCC 填料进行造纸的可能性

Kimmo Koivunen and Hannu Paulapuro

15 COMPUTER SIMULATION

Prediction of handsheet tensile strength by computational simulation of structure

Previsão da resistência à tensão da folha manual através de simulação computacional da estrutura

利用结构的计算模拟预测手抄纸的抗张强度

Rémi Vincent, Martine Rueff, and Christian Voillot

20 WASTEWATER TREATMENT

Characterizing carbonaceous biochemical oxygen demand load reductions from pulp and paper mills for activities related to total maximum daily loads

Caracterização das reduções de carga com demanda bioquímica de oxigênio contendo carbono, proveniente das fábricas de celulose e papel para atividades relacionadas às cargas totais máximas diárias

对浆粕造纸厂的每日最大总负荷的相关活动的碳质生化需要量负荷降低的定性

James E. Palumbo and Linfield C. Brown

27 COATING

Calendering effects on coating pore structure and ink setting behavior

Efeitos da calandragem na estrutura dos poros do revestimento e comportamento da fixação da tinta

压光对涂层微孔结构以及油墨固着行为的影响

Peter Resch, Wolfgang Bauer, and Ulrich Hirn

»THIS MONTH'S COVER IMAGE: AERIAL PHOTO OF PAPER MILL EFFLUENT SETTLING PONDS BY ISTOCK INTERNATIONAL.

TAPPI, 15 Technology Parkway S., Norcross, GA, 30092, publishes *TAPPI JOURNAL* monthly.

Editor's Note

MONICA SHAW | EDITORIAL DIRECTOR
mshaw@tappi.org

Moving forward

I would like to take this opportunity to introduce myself as the new Editorial Director of *TAPPI Journal*. First, I would like to express what an honor it is to be a part of *TJ* and work with the dedicated experts on its Editorial Board to provide TAPPI members with a peer-reviewed journal that advances science and improves processes in paper and related industries. Next, I want to acknowledge Jan Bottiglieri, *TJ*'s previous editor, for her hard work and service to TAPPI and *TAPPI Journal*. I know *TJ* readers will miss her input.

As for my own background prior to joining *TAPPI Journal*, I have a B.S. in Computer Science with a concentration in Mathematics, as well as an M.A. in English. Professionally, I have held various technical writing roles in the aerospace and software industries, as well as editorial roles with *Pulp & Paper* magazine, where I worked for 11 years, serving as Editor from 2001-2007. I look forward to employing my skills and background in science with *TJ*, but I also am looking for your suggestions, comments, and participation as we move ahead.

No stranger to change

For more than 90 years, *TAPPI Journal* has been a preferred source of peer-reviewed papers. The journal's name has changed over time, as has its format and content, but the commitment remains the same: to provide unique and useful scientific insights for TAPPI members.

As a TAPPI member, you have likely noticed an increased emphasis within TAPPI on providing information, networking, and event opportunities for an increasingly diverse, yet related, set of communities served through various divisions and committees. These communities include nonwovens, both flexible and corrugated packaging, bioenergy, engineering, management, coating and graphic arts, product quality, and process control, as well as pulp, paper, board and tissue.

Going forward, *TJ* will reflect the changes within TAPPI itself with a broader range of content that addresses the rapidly changing research landscape of those diverse, but connected industries. We will work to provide increased content on emerging fields like nanotechnology, the biorefinery, and nonwovens, while maintaining coverage of core pulp, paper, and tissue topics.

Going forward, *TJ* will reflect the changes within TAPPI itself with a broader range of content that addresses the rapidly changing research landscape of diverse, but connected industries.

Looking for SMEs

There is a long standing invitation for qualified subject matter experts (SMEs) among TAPPI's membership to participate in the peer review process. As the paper industry continues to change significantly in coming years, this participation is more important than ever. Your input in any of the following areas would serve to both improve *TJ* and address the larger goal of advancing science in our industry:

- All pulping and papermaking processes
- Tissuemaking
- Bioenergy
- Nanotechnology
- Corrugated Packaging
- Printing
- Nonwovens

Becoming a *TAPPI Journal* peer reviewer allows you to preview some of our industry's most important new research while sharing your knowledge with the industry's community. To volunteer or offer suggestions for *TJ*, please send your contact information and areas of expertise to me at mshaw@tappi.org. Your input is greatly appreciated.

Monica Shaw
Editorial Director, *TAPPI Journal*

Papermaking potential of novel structured PCC fillers with enhanced refractive index

KIMMO KOIVUNEN AND HANNU PAULAPURO

ABSTRACT: While much effort has been focused on optical properties imparted by particle size distribution, shape, and packing of inorganic particles, the refractive index contrasts within the paper matrix have received less attention. PCC fillers can be used as tools for increasing the refractive index contrast, which further improves paper optical properties. We studied the papermaking potential of novel PCC fillers with an enhanced refractive index. PCC samples were fabricated by conventional carbonation method in the presence of refractive-index enhancing additives. We had previously found that introduction of ZnO as fine spots, including nano-sized structures, on host PCC surfaces improved the effective refractive index and optical performance of PCC. Now, we have studied the papermaking potential of this approach in experiments with handsheets using moderate Zn modification. In addition to Zn, we studied the effect of Sr as an additive and found that Sr inclusion alters the host particle morphology and crystal structure. We report effects of such modifications on light scattering coefficient, brightness, opacity, tensile strength, bulk, and porosity of paper, both before and after calendering. Our results suggest beneficial optical properties, as well as combination of light scattering with strength properties, especially in the case of Sr modified filler. Zn modified fillers opened the sheet structure, while Sr structuring closed the sheets. Calendering resulted in reduced bulk with all fillers, while optical properties were maintained with the Sr modified PCC, but reduced benefit was observed in the combination of light scattering and strength. Calendering conditions should therefore be optimized for these fillers. A higher modification degree of the fillers should also be considered to achieve a more significant refractive index contrast.

Application: We found a practical method to introduce refractive index contrasts on PCC filler particle surfaces. This can be utilized to improve paper optical properties.

Light scattering occurs both in the fibrous base paper and in the coating layer matrices. One of the main functions of fillers and coating pigments is to boost light scattering of the matrices. Light scattering from filler and coating pigments depends on the particle size distribution, specific surface area (SSA), flocculation, and refractive indices of the particles. The resulting pore size distribution of the surrounding media is also important. The floc structure, influenced by the particle shape, affects the number and size of the pores [1].

Introduction of filler into paper usually takes place by mixing the filler with the fibrous stock prior to the forming stage. In a paper web produced by such a typical process, filler pigments affect light scattering through two mechanisms: by increasing the specific surface area of the matrix, and by preventing bonding between fibers. These effects were suggested by Hemstock [2], Alince and Lepoutre [3], who have further demonstrated the separation of these effects, and proposed that the role of fiber debonding in light scattering decreases as the refractive index of the filler increases.

Fillers can be located either on the free fiber surfaces or in the pores formed by the surrounding fibers without significant effects on the structure of the fibrous network itself [4]. Fillers can also be located at the crossings of adjacent fibers [4], which causes debonding and significantly reduced tensile strength.

Proper particle size of fillers and pigments is essential for achieving optimum light scattering. As suggested by Bown [5], particle size should be considered together with size distribution, density, and aggregate properties. The effective particle size is about half a wavelength of light and the particles should have narrow size distribution around this size class. The same is true for the pore size distribution [6], which is also affected by properties of filler or pigment particles. Work done by Alince et. al [7], suggests that when porosity provided only by such optimal pores is examined, and all particles display similar refractive indices, linear dependence between light scattering and porosity can be found. Work completed by Silenius [8] demonstrates how certain filler-fiber composites ("SuperFill" technology) can be utilized to boost the light scattering effect of filled sheets. This technology is thought to contribute to light scattering by providing less flocculated distribution of filler and by its ability to yield advantageous paper pore structure.

A low degree of particle flocculation contributes to light scattering but increases sheet debonding. Particulate retention requires controlled flocculation. Flocs can be formed among filler particles alone through homoflocculation [9, 10], or together with fines through heteroflocculation [11]. Low retention of fillers negatively affects papermaking, for example, by increasing sizing agent consumption. Therefore, to ensure development of paper's mechanical properties and

paper machine runnability, fillers may be introduced to paper as flocs. However, this approach reduces light scattering, as has been extensively documented in the literature. For example, according to Holm [9], preflocculation leads to improved sheet strength at the expense of optical properties.

It is possible to improve optical properties without sacrificing sheet strength by increasing the filler content in paper. A study conducted by Subramanian, et al., [12] suggests that filler contents up to 50%-60% can be achieved using fiber-filler composites in which PCC particles have been introduced on fine cellulosic material. Progress in micro- and nanocellulose technologies may provide new opportunities for papermakers to use such fillers.

In contrast to changing the particle size, specific surface area, or filler content, refractive index manipulation has not been exhaustively investigated. There are limits on decreasing particle size or increasing specific surface area beyond which light scattering starts to decrease. This applies to pore size as well. Further, retention sets another limit for reducing particle size. Filler effects on mechanical properties of paper and runnability of paper machine limit the filler contents. Such limits, however, do not concern refractive index. If other parameters are fixed, increasing the refractive index differences of optical interfaces always increases light scattering in a sheet. As the refractive index of most of the current papermaking materials is close to 1.6, significant improvement in light scattering can be achieved with refractive index values of around 2.0 by utilizing innovative colorless composite structures. This is an issue for investigation, as the lack of refractive index differences on the solid-solid interfaces of paper characterizes the majority of paper grades of the day. In a typical fibrous paper matrix, light scattering takes place mainly on solid-air interfaces.

In ray optics, effect of refractive index on the interaction between a light beam and transparent material (**Fig. 1)** can be described by Snell's law according to Equation (1),

$$n_1 \sin \Theta_1 = n_2 \sin \Theta_2 \qquad (1)$$

where n_1 and n_2 represent the refractive indices of the two media.

Furthermore the degree of bending of light, refractive index affects the intensity of the reflected light beam. The importance of refractive index differences on optical interfaces on this reflection can be understood from Fresnel equations,

$$R_s = \left[\frac{n_1 \cos(\Theta_1) - n_2 \cos(\Theta_2)}{n_1 \cos(\Theta_1) + n_2 \cos(\Theta_2)}\right]^2 \qquad (2)$$

$$R_p = \left[\frac{n_1 \cos(\Theta_2) - n_2 \cos(\Theta_1)}{n_1 \cos(\Theta_2) + n_2 \cos(\Theta_1)}\right]^2$$

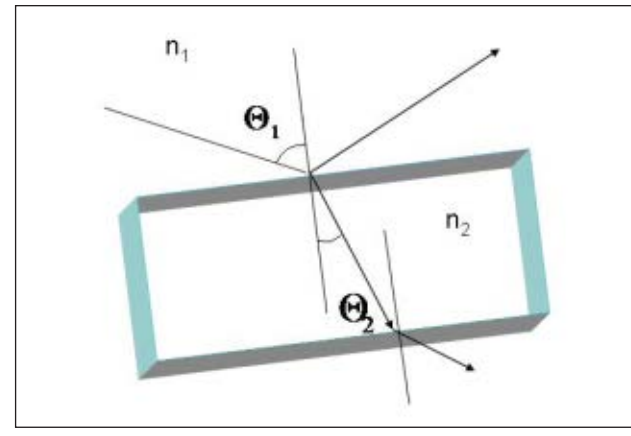

1. Interaction between light and transparent material.

where R_s and R_p are reflection coefficients for light polarized in two planes. The Fresnel equations are valid only for even surfaces. They show the effect of the refractive index of material on the intensity of specular reflection or gloss. In practice, the occurrence of micro-roughness reduces specular reflection and increases diffuse light scattering. On particle distances that are in the order of magnitude of wavelength of light, such as in a coating matrix, a wave optical approach, based directly on Maxwell's equations, should be used instead of the ray optical description [13].

The refractive index of material depends on its molecular constitution. Refractive indices of organic materials, including cellulose, are usually around 1.5-1.6 [14]. The nature of chemical bonding has an important role for development of refractive index. Chemical bonding in high volume fillers and pigments, such as carbonates and silicates, are characterized by low degree of covalence, and consequently low degree of specific refractivity [15]. Covalence of bonding affects the electron density, which is a major contributor for refractive index of a material, as equation (3) indicates [16],

$$n = 1 + \frac{N q_e^{\,2}}{2\varepsilon_0 m\left(\omega_0^{\,2} - \omega^2\right)} \qquad (3)$$

with these values:

n	refractive index
N	number of charges per unit volume
q_e	charge of electron
ε_0	permittivity of vacuum
m	mass of electron
ω	angular frequency of radiation
ω_0	resonant frequency of electron

More specific descriptions on refractive indices of media can be found in the literature [17]. Combinations of high-volume pigments and specialty pigments are often replaced with modified high-volume pigments to boost paper performance [1, 18].

The industry is actively investigating the beneficial effect provided by nanotechnology. For example, a modified calcium carbonate with nano features has a positive effect on pigment-ink interaction [19]. As shown by Schoelkopf et al. [20, 21], Gane et al. [22] and Ridgway et al. [23], a discrete pore structure, provided by the modified calcium carbonate, contributes to rapid liquid absorption and high liquid uptake. This can be further utilized in printing paper applications. The fraction of GCC in GCC-clay coatings may be raised due to continually increasing demand for high brightness. The surface structure of GCC pigments can be modified to enable sufficient coating structuring with GCC alone [24]. A recent study by Koivunen et al. [25] introduces a novel ZnO-nanostructured PCC with an increased refractive index, birefringence, and light scattering potential. In this study we have examined the papermaking potential of PCC with moderate ZnO and $SrCO_3$ modifications.

Materials and methods

We fabricated PCC samples in laboratory by carbonation, i. e., feeding carbon dioxide gas into slurry of slaked milk of lime. In this process we fabricated (a) a reference PCC, referred to as "S-PCC", with clustered scalenohedral (rosette-like) particle morphology, and (b) three structured PCC samples (Nano-S-PCC): (b1) two PCC with light Zn based, and (b2) a PCC with a Sr-based modification. Formation of calcium carbonate takes place according to equation (4):

$$Ca(OH)_2 + CO_2 \rightarrow CaCO_3 + H_2O \quad (4)$$

PCC fabrication by carbonation has been thoroughly explained, for instance, by Silenius [8]. To form light scattering structures displaying refractive index contrasts on the PCC surface, soluble Zn and Sr compounds were used as additives during the reaction. A more detailed description of the structured PCC fabrication has been published elsewhere [25].

Samples were filtered, washed with deionized water, dried, and prepared for further analyses. One commercial scalenohedral PCC, referred to as "S-PCC (Com)," was also used as a reference. Particle size distributions of the fillers were determined with a Beckman Coulter LS 13 320 particle size analyzer.

To document the realized chemical composition of samples, we conducted thermal gravimetric analyses (TGA) using a Netzsch STA 449C device, combined with a capillary to Netzsch QMS 403C mass spectrometer. Sample size was about 10 mg, and helium was used as a protective gas. The flow rate of the protective gas was 70 mL/min. The testing samples were heated in Al_2O_3 crucibles up to 1,250 °C, with a heating rate of 10 K/min. Released gases were analyzed in the mass number range of 2-300.

The crystal structure of the Sr modified sample was analyzed by x-ray diffraction measurement. X-ray diffraction patterns were collected with a Philips PW1710 device using Cu K_α radiation. XRD analysis of zinc modified samples has been reported earlier [25]. The specific surface area (SSA) was measured with a Micrometrics FlowSorp II 2300 analyzer by determining the adsorbed and desorbed nitrogen, utilizing the BET (Brunauer, Emmet, and Teller) theory.

Component	Point of addition, s (after addition of the fibrous stock)	Dosage, mg/g
Starch	11	5
Filler	30	Determined by target filler content
Retention Aid	40	200

I. Addition of chemicals in handsheet preparation with MBF.

Dried birch and pine chemical pulp sheets from Finnish pulp mills were soaked in water and mixed to achieve 70/30 birch/pine fine paper furnish mix. The furnish was beaten with a Valley Hollander to °SR 18 in accordance with the Standard SCAN-C 25:76 and diluted to 3 g/l consistency for handsheet preparation. The pH and temperature of the stock were around 7 °C and 20 °C, respectively. Dry-strength starch (Raisamyl 50021) was cooked in 95 °C for 25 minutes prior to handsheet preparation. Fillers were dispersed with a Diaf mixer and then continuously stirred with a magnetic stirrer. Fennopol K 3400R was used as a retention agent. Handsheets of 80 g/m² were prepared with Moving Belt Former (MBF) drainage testing and sheet forming apparatus [26]. First, the fibrous stock was added in to the container of the MBF. Chemicals were then added in order as shown in **Table I**.

The procedure of chemical addition was intended to mimic the wet end operations of a typical paper machine environment. The stock in the container was continuously mixed with a propeller mixer. Target filler contents of the handsheets were 15 wt%, 25 wt%, and 35 wt%, with ±1.5 wt% unit deviation. Formed wet sheets were couched from the wire, wet-pressed and drum-dried. The sheets were then stored in accordance with the Standard SCAN-P 2:75 and finally tested with Standard Methods. Sheets were calendered through a single nip on an EP-210 laboratory calender using 70 kN/m line loads, 70°C hot roll surface temperature, and 35 m/min speed.

Micrographs were taken and elemental mapping was implemented for handsheets with SEM and EDS, respectively. The aim was to observe the presence of the structures carried by the host PCC particles in a paper web to verify that they had been retained. A piece of paper was attached on a sample base with two-sided tape and coated with gold, using a 15.0 kV accelerating voltage.

Sample	Cluster size, µm		SSA, m²/g	ZnO, w-%	$SrCO_3$, w-%	SrO, w-%	n_{eff}
	Mean	Median					
S-PCC	7.380	7.273	5.6	-	-	-	1.58
S-PCC (Com)	4.099	3.567	6.4	-	-	-	1.58
Nano-S-PCC 1	7.989	7.748	6.2	1	-	-	1.582
Nano-S-PCC 2	5.940	5.781	8	8	-	-	1.597
Nano-S-PCC 3	4.341	3.823	10.5	-	3.5	1	1.578*

** the value is based on the assumption that $CaCO_3$ is in the form of calcite. Presence of aragonite was later observed, and this effect is discussed below.*

II. Characterization of the fillers.

RESULTS AND DISCUSSION

Table II presents the average particle size: more precisely, cluster size, SSA, TGA (additive content), and calculated refractive index data from the PCC samples. The S-PCC reference together with the Nano-S-PCC 1 exhibited the coarsest cluster size. The Nano-S-PCC 3 occurred as finer clusters and is hence more comparable with the size of the other reference, S-PCC (Com). All structured samples were moderately modified. The chemical composition of the structured samples was assessed from the TGA measurements.

From TGA data, the effective refractive index (n_{eff}) of a composite pigment consisting of a host particle (h) and a coating layer of particles (c) can be approximated from the refractive indices (n) and the volume fractions (V) of the host and the particle layer, respectively, according to equation (5). The same formula has been used in immersion liquid-based measurements of refractive index of PCC, which have been described earlier [25]:

$$n_{eff} = \frac{V_h n_h + V_c n_c}{V_h + V_c} \quad (5)$$

Using the densities and refractive indices of ZnO (5.606 g/cm³ and 2.0, respectively [27]), and $SrCO_3$ (3.7 g/cm³ and 1.516, respectively [27]), we have calculated the effective refractive indices accordingly (Table II). Density and refractive index of calcium carbonate (calcite) used in the calculation are around 2.71 g/cm³ and 1.58, respectively [27].

Figure 2 presents the TGA curve of the Nano-S-PCC 3 sample. The decomposition of $CaCO_3$ can be observed as steep weight loss around 600 °C – 700 °C. The minor loss occurring in 800 °C is due to decomposition of $SrCO_3$. Our assumption is based on the detected release of CO_2 gas. The remaining trace of strontium is expected to occur in the form of an oxide. Our XRD study indicated occurrence of aragonite together with calcite in the Nano-S-PCC 3 sample. The presence of aragonite (n=1.63) suggests that the refractive index must be higher than that calculated from Table II, in which the n value of 1.58 for calcite is used [27]. Because precise fractions of calcite and aragonite in the sample remained unclear, we decided to use the estimate $1.58 \leq n_{\text{Nano-S-PCC3}} \leq 1.63$ for this sample.

Figures 3-4 show micrographs of ZnO modified PCC samples. ZnO structures can be distinguished in the backscattering images (Fig. 4) as bright spots on the surface of PCC particles. For visualization, the structure contents in the samples presented in Fig. 3 are higher than examined elsewhere in this study. Figure 3 should be considered as a guide, illustrating the structured PCC concept. The reference PCC, typical scalenohedral calcite, is shown in **Fig. 5** (left). Effects of

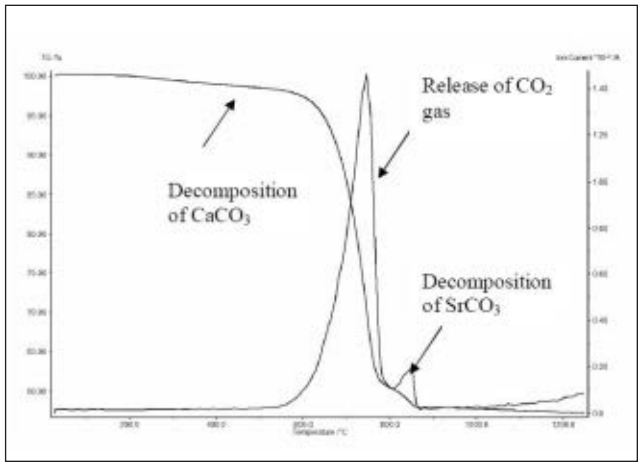

2. Thermal analysis of the Nano-S-PCC 3 sample.

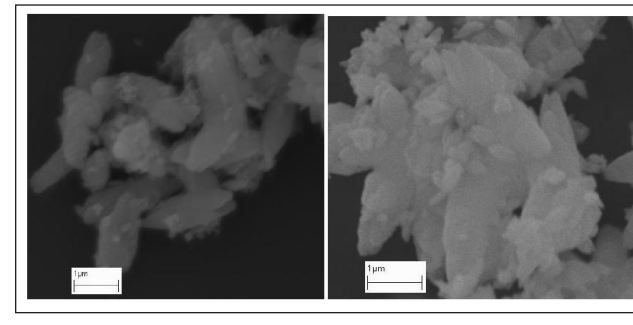

3. PCC samples with 10 w-% (left) and 18 w-% (right) Zn structure content.

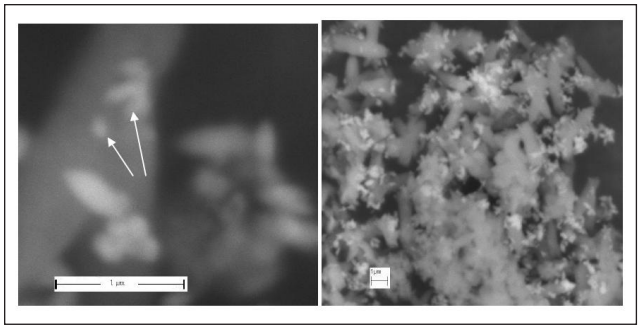

4. ZnO particles on the PCC surface. Backscattering images. Nano-sized structures (≤ 100 nm) are marked with arrows.

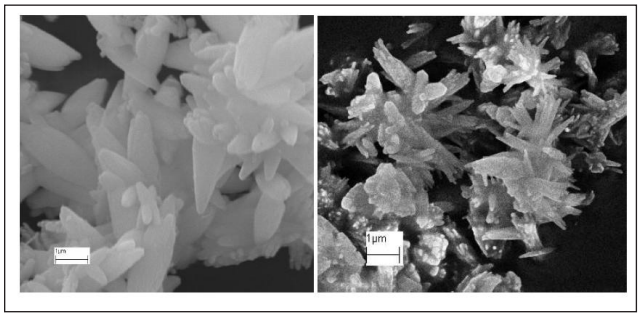

5. Reference PCC (left) and PCC with 3.5 w-% $SrCO_3$ content (right).

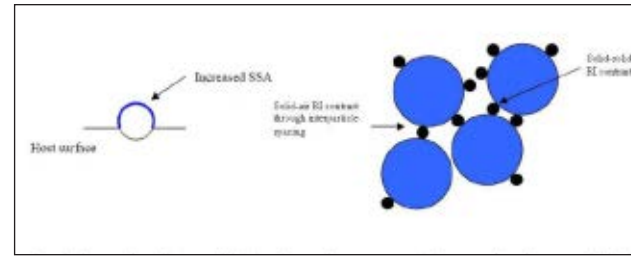

6. Schematic figure illustrating the suggested mechanisms of light scattering generation through the novel filler. Left: increased specific surface area due to the fine particle. Right: spacing effect and refractive index contrasts occurring in a filler aggregate.

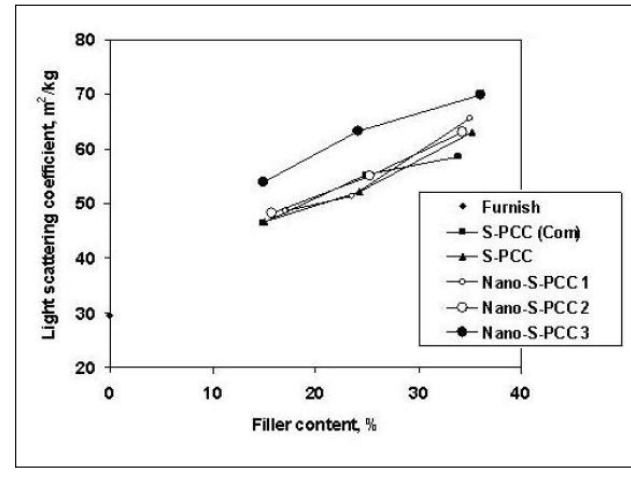

7. Effect of filler type on the light scattering coefficient of the handsheets.

Sr can be observed both as bright spots and altered host particle morphologies (image on the right). EDS elemental mapping conducted for the sheets provided evidence that the Zn-based structures had been retained in the handsheets. Presence of these structures may affect both filler packing and refractive index contrasts present in the sheet. Therefore, in the following, we discuss such effects with respect to light scattering generation.

Packing of filler particles plays a critical role in the development of light scattering. The refractive index gamut associated with a filler system should be considered together with packing density. With the structure containing fine ZnO particles, illustrated in **Fig. 6**, our approach was to provide improved optical sheet performance, compared to conventional fillers, through the following distinctive mechanisms.

First of all, the Zn based nanostructures provide local refractive index contrast to the PCC host particles. As presented in Fig. 4, some of the structures are nano-sized (≤100 nm). Tailoring the refractive index of various nanocomposites has gained attention in the field of optical physics [28-34]. The light scattering provided by such nanoparticles has been discussed in an ellipsometric study completed by using our fillers and various nanoparticles [35]. The light scattering is boosted by local index mismatches introduced by such particles.

Second, in our case, particles with size class 100-500 nm are also present. Uneven surface topography of the structured fillers therefore can be expected to affect diffuse scattering. Incorporated particles raise the specific surface area, which consequently leads to an increase in interparticle spacing between host particles. In optics, interparticle spacing that displays no less than 200 nm distance between (host) particles makes the most significant contribution to light scattering. Packing should, therefore, be controlled to obtain effective interparticle pore size. Limited contact between particles is most attractive and attention to pore size distribution is critical.

The importance of spacing of high-refractive-index pigments has also been recently presented by Holm [36], while spacing technology through fine particles in GCC coatings has been presented by Gane [24]. When packing density increases throughout a sheet of paper; e.g., by calendering or locally by filler particle flocculation [9, 10], a high number of interparticle contacts form and, consequently, solid-solid interfaces replace solid-air interfaces. This decreases refractive index contrasts and reduces light scattering [9]. As presented by Gavelin [11], similarly in heteroflocculation, fillers form flocs together with fines. From the optics viewpoint, formation of solid-solid contacts is similar, since fines and fillers have similar refractive indices. The light scattering effect decreases when particles are assembled in distances below 200 nm from each other. Flocculation and local close packing are necessary to achieve sufficient retention. Col-

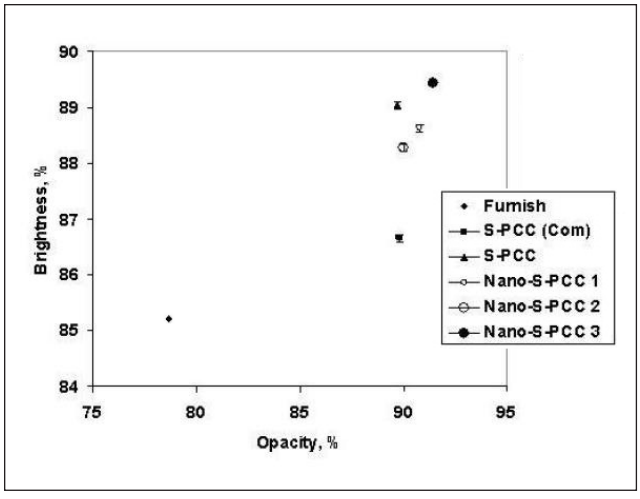

8. Effect of filler type on optical properties of the handsheets. 80 g/m² grammage, 35 w-% filler content.

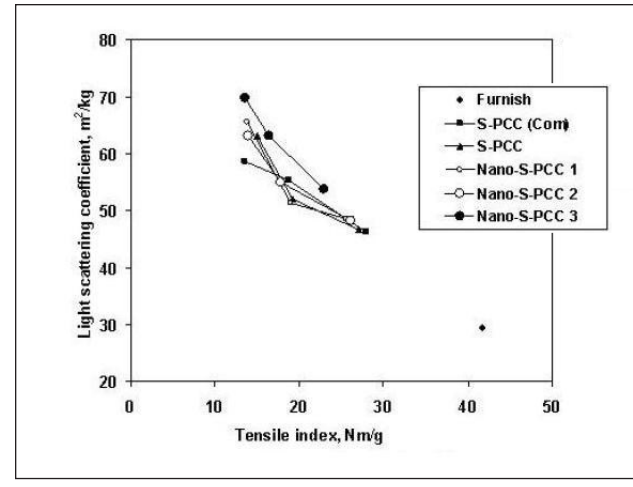

9. Light scattering coefficient against tensile index of handsheets.

lapsing of the particle structure may also occur upon calendering. Therefore, it is beneficial that not all particles in a floc display similar indices.

The fourth mechanism we suggest is related to the distribution of nanoparticles on host particles. When considering an ordinary blend consisting of typical filler particles and very fine additional particles, separation between two particle types may take place due to colloidal interactions within the fraction of fine particles. Segregation of two filler types with differing morphologies has been explained earlier in detail by Gane et al. [18]. When the particles are attached onto the host particles, such separation is prevented and the number of solid-solid contacts displaying refractive index contrast is maximized.

Fine structures, such as observed in the case of Zn based modification, are also present in the case of Sr modified PCC (Fig. 5). In addition, the host particles themselves display a different, needle-like, structure. Such a structure is characteristic of aragonite carbonates. This might be an indication of an additional Sr incorporation in the host particles. Such incorporation may have taken place through a substitution mechanism. According to V.M. Goldschmidt [15], substitution of ions in a crystal may take place if the size of the substitute does not differ from the size of the original ions by more than 15%. The size of Sr is close to that of calcium; hence such a mechanism could work. The presence of Sr has been observed to contribute to aragonite formation. In fact, strontium yields more stable aragonite than calcium [37].

Figure 7 shows the light scattering coefficient as a function of filler content with different fillers. Our samples display various cluster sizes, which obviously must be considered in this context. For instance, as presented in Table II, Nano-S-PCC 3 displays smaller cluster size than Nano-S-PCC 1 (or Nano-PCC-2) but is close to that of the commercial reference PCC. Nano-S-PCC 3 yields the highest light scattering of the fillers, including the reference, hence other parameters must also be considered. The shape of Nano-S-PCC 3 significantly differs from that of the other samples, and can be hence expected to result in different packing and pore structure of the sheet. These factors, together with different refractive indexes, may explain most of this behavior. The influence of crowding [3]; i.e., leveling of the light scattering with high filler content, can be envisioned in the case of Nano-S-PCC 3. This might be due to the high packing density. Nano-S-PCC 3 also yields the best combination of paper brightness and opacity, as shown in **Fig. 8**.

No benefits in optical properties were observed with Nano-S-PCC 1 or Nano-S-PCC 2. A probable reason for this is the very low content of ZnO particles. **Figure 9** suggests the contribution of the Nano-S-PCC 3 filler on both the light scattering coefficient and tensile index. Particle size affects both optical and strength properties and can influence combinations of the two. As suggested by Bown [5], small particles sized approximately 2 µm can yield better combinations than large particles (6 µm). If we assume that the cluster size has a similar effect in our case, this could explain results here, in addition to the effect discussed in the context of light scattering.

The refractive index contrast should be discussed together with packing density. As illustrated in **Figs. 10-11**, Nano-S-PCC1 and Nano-S-PCC2 yield increased bulk and especially air permeability, respectively, which might be an indication of the spacing effect discussed above. Nano-S-PCC3 yields low bulk and air permeability, suggesting high packing density. This could be expected due to the relative higher density and aspect ratio of aragonite. Differences however in the particle sizes between samples must also be considered.

Figures 12-15 show the effect of calendering. Calendering typically reduces pore volume and can therefore affect light scattering. After calendering, Nano-S-PCC 3 maintains a competitive degree of light scattering. The advantage of light scattering and strength properties observed with uncalendered sheets has been reduced. Nano-S-PCC 3 provided the most closed sheet structure. The beneficial light scattering

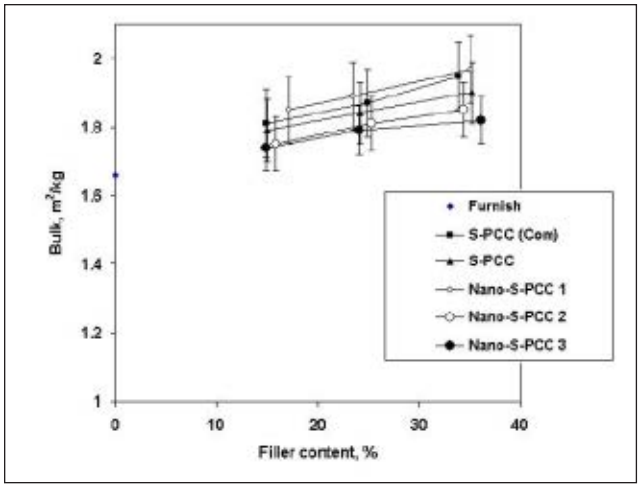

10. Bulk against filler content of the handsheets.

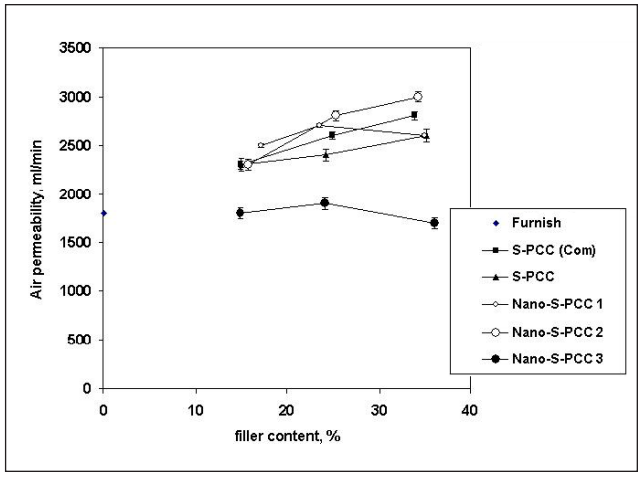

11. Air permeability against filler content of the handsheets.

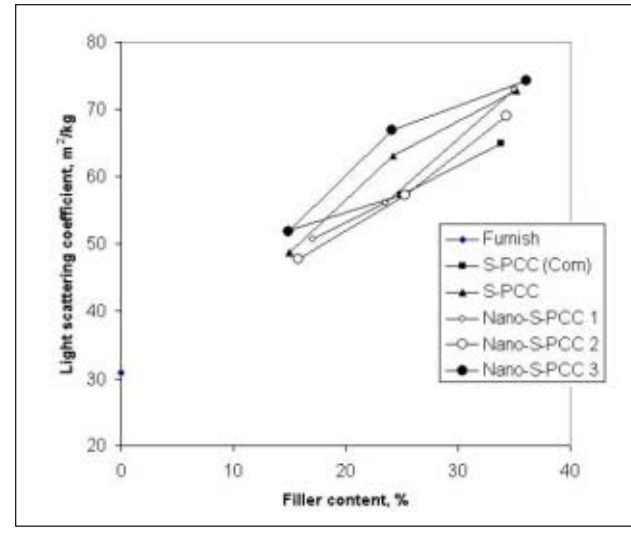

12. Effect of filler type on the light scattering coefficient of the handsheets. Calendered sheets.

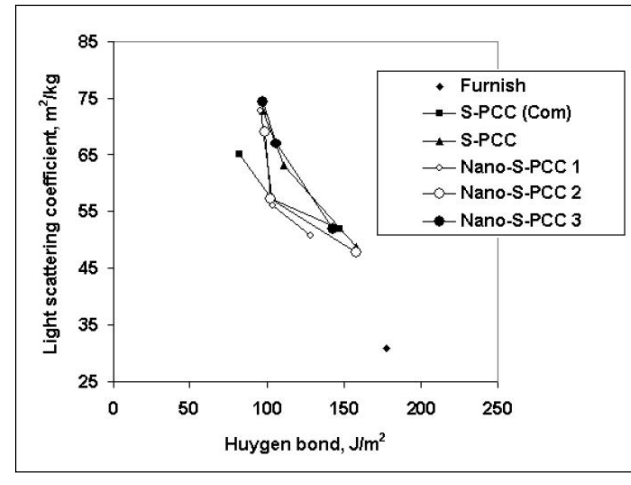

13. Light scattering coefficient against Huygen bond of the handsheets. Calendered sheets.

could be an indication that all pores which scatter light have not been totally collapsed. However, details of pores have not been examined and, accordingly, this is only a presumption.

CONCLUSIONS

The objective of this study was to test the papermaking potential of novel structured PCC fillers with enhanced refractive index. Considering the economic feasibility of such an approach, we examined only moderate structuring. Structuring comprised introduction of optically effective fine particles on conventional scalenohedral PCC host particles with or without host particles' shape modification. The nature of structuring was controlled by chemical modification. Zn was introduced in fine particles form only, while Sr was introduced by changing the host particles' shape to a more needle-like configuration.

Our results indicated acceptable optical properties and combination of optical-strength properties, especially in the case of Sr-based structuring. After calendering, beneficial light scattering was still observed, while property balance reduced the advantage. Introduction of Zn-based structures did not produce improved paper optical properties, probably due to the low structural content.

Our observations suggest easy processing and preparation of the modified fillers. These fillers can be introduced into paper in the wet-end and will yield competitive paper properties. The (nano)-structured fillers behave mostly as regular fillers without disturbances or adverse effects. Results complement our earlier findings and provide novel information regarding the good papermaking potential of (nano)-structured fillers. Modification of the fillers should, however, be high enough to realize beneficial paper optical properties. Optimization of calendering conditions must also be considered. **TJ**

ACKNOWLEDGEMENTS

Financial support from the Finnish Funding Agency for Technology and Innovation (TEKES), J.M. Huber Finland Oy, M-Real Oyj, Omya Oy, and UPM-Kymmene Oyj is gratefully appreciated.

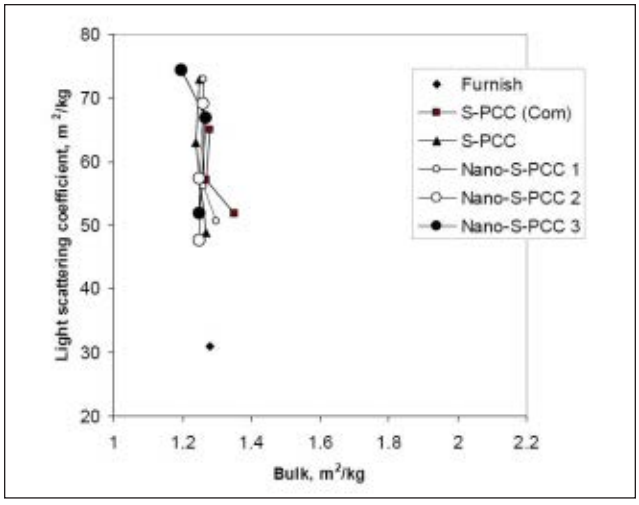

14. Light scattering coefficient against bulk. Calendered sheets.

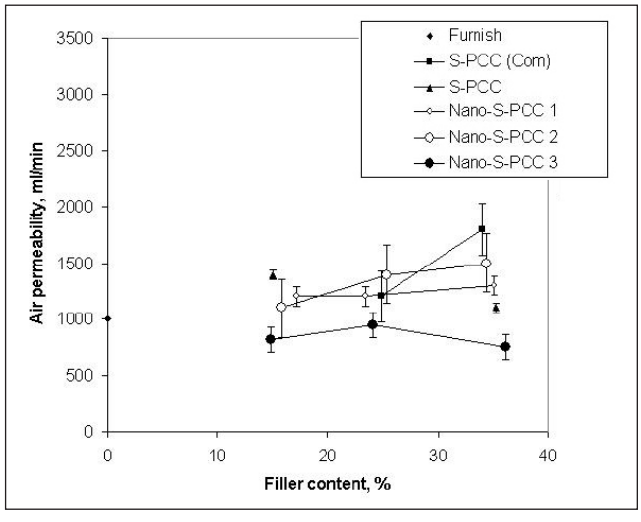

15. Air permeability against filler content of the handsheets. Calendered sheets.

LITERATURE CITED

1. Laufmann, M. in *Handbook of Paper and Board* (H. Holik, Ed.), Wiley-VCH Verlag GmbH&Co., Weinheim, 2006, pp. 33-61.
2. Hemstock, G.A., *Tappi* 42(2): 158 A (1962).
3. Alince, B. and Lepoutre, P., *Tappi J.* 68(4): 122(1985).
4. Weigl, J., Zeuner, M., and Baumgarten, H.L., *Papier* 35(10A):V46 (1981).
5. Bown, R., *Pira International Conference on Use of Minerals in Papermaking 1997*, Pira publications, Manchester, UK, p. 62.
6. Pauler, N., *Paper Optics*, AB Lorentzen & Wettre, Kista, p. 75.
7. Alince, B., Porubska, J., and Van de Ven, T.G.M. *J. Pulp Paper Sci.* 28(3): 93(2002).
8. Silenius, P., "Improving the combinations of critical properties and process parameters of printing and writing paper and paperboards by new paper-filling methods," Ph.D. thesis, Helsinki University of Technology, Espoo, 2002.
9. Holm, M., and Manner, H., 28th *DITP International Annual Symposium 2001*, Bled, Slovenia, p. 167.
10. Porubska, J., Alince, B., and van de Ven, T.G.M., *Colloids Surf.* 210(2-3): 223(2002).
11. Gavelin, G., Pat. EP0270103 (1998).
12. Subramanian, R., Forsmand, H., Paltakari, J., et al., *J. Pulp Paper Sci. 34(3): 146(2008).*
13. Keller, F.J., Gettys, W.E., and Skove, M.J., *Physics: Classical and Modern*, 2nd ed. McGraw-Hill, New York (NY), 1993, p. 877.
14. Seferis, C.J., in *Polymer Handbook* (Brandrup, J., Ed.), 4th Edition, Wiley, New York, 1999, p. 571.
15. Jaffe, H.W., *Crystal Chemistry and Refractivity*, 2nd Edition, Dover Publications, Mineola, New York, 1996.
16. Feynman, R. P., Leighton, R.B., and Sands, M., *The Feynman Lectures on Physics: Commemorative Issue, Vol. 1: Mainly Mechanics, Radiation, and Heat*, Reading, MA, 1989.
17. Peiponen, K.E., Vartiainen, E.M., and Asakura T., *Dispersion, Complex Analysis and Optical Spectroscopy*, Springer, Heidelberg, 1999.
18. Gane, P.A.C., Buri, M., and Blum, R., *The International Symposium on Paper Coating Coverage Proceedings*, Helsinki, 1999, p. 2.
19. Ridgway, C. J., Gane, P.A.C., and Schoelkopf, J., *Transp Porous Med* 63(2): 239(2006).
20. Schoelkopf, J., Gane, P.A.C., Ridgway, C.J., et al., *Nordic Pulp Paper Res. J.* 15(5): 422(2000).
21. Schoelkopf, J., Ridgway, C. J., Gane, P.A.C., et al., *J. Colloid Interface Sci.* 227(1): 119(2000).
22. Gane, P.A.C., Ridgway, C.J. and Schoelkopf, J., *Transp Porous Med* 54(1): 79(2004).
23. Ridgway, C. J. and Gane, P.A.C., *Colloids Surf. A* 206(1-3): 217 (2002).
24. Gane, P.A.C., *TAPPI 1998 Coating/Papermakers Conference*, New Orleans, p. 807.
25. Koivunen, K., Niskanen, I., Peiponen, K.E., et al., *J. Mater Sci.* 44(2): 477(2009).
26. Räisänen, K., "Water removal by flat boxes and a couch roll on a paper machine wire section," Ph.D. thesis, Helsinki University of Technology, Espoo, Finland, 1998.
27. Lide, D.R., *CRC Handbook of Chemistry and Physics: A Ready-Reference Book of Chemical and Physical Data*, 71st ed., Boca Raton, CRC, 1990.
28. Zeng, X.C., Bergman, D.J., Hui, P.M., et al., *Phys. Rev. B* 38: 10970(1988).
29. Shalaev, V.M., *Optical Properties of Nanostructured Random Media*, Springer, Heidelberg, 2002.
30. Aspnes, D.E., *Am. J. Phys.* 50: 704(1982).
31. Chylek, P. and Videen, G., *Opt. Commun.* 146: 15 (1998).
32. Lakhtakia, A., *Opt. Commun.* 192: 145(2001).
33. Scaffardi, L. B. and Tocho, J. O., *Nanotechnology* 17: 1309(2006).
34. Boyd, R. W. and Sipe, J. E., *J. Opt. Soc. Am.* B 11: 297(1994).
35. Juuti, M., Koivunen, K., Silvennoinen, M., et. al., *Colloids Surf. A* 352: 94(2009).
36. Holm, M., *Fillers and Pigments for Papermakers 2007*, Pira International, Berlin, p. 20.
37. Klein, C. and Hurlbut, C. S., *Manual of Mineralogy (After James D. Dana)*, 21st edition, John Wiley & Sons, New York, 1999.

INSIGHTS FROM THE AUTHORS

Fillers are added to paper stock to improve optical properties and to reduce costs, but they also have negative effects on paper properties, which limit their use. Accordingly, fillers must be optimized to achieve the best balance. This may be accomplished by changes in filler particle size, shape, specific surface area, or refractive index. The last of these possibilities has received the least attention.

We considered this topic of high relevance and, in 2006, launched a multidisciplinary three-year project called "Nanopap" together with our financiers and research partners. Our objective was to increase the refractive indices of various fillers and coating pigments by technically and economically feasible means, including nano-scale modifications.

In our studies, we have observed significantly increased refractive indices and improved optical performance, as well as beneficial combinations of optical and strength properties. Our findings may point to further potential for efficient use of materials. For example, PCC could be used as a platform to introduce refractive index contrasts in paper. The challenge is to introduce contrasts that can be realized in improved paper performance without excessive increase in material costs. An approach we present in this paper is attaching them to host filler particles. More research in the usability and economics of novel fillers is needed.

Koivunen

Paulapuro

Koivunen is a research scientist and Paulapuro is a professor of paper and printing technology, School of Science and Technology, Aalto University, Espoo, Finland. For more information, email kimmo.koivunen@tkk.fi.

Prediction of handsheet tensile strength by computational simulation of structure

RÉMI VINCENT, MARTINE RUEFF, AND CHRISTIAN VOILLOT

ABSTRACT: To better understand the influence of fiber morphology on paper properties, we developed a novel 3-D computational simulator of paper structure, which was validated through experimental work. This simulator creates virtual pieces of handsheets using the size distributions of the fibers as the main inputs. Once the structure is generated, physical properties can be assessed. The main principles of the simulation and the results for one global texture property, the apparent density, were presented in a previous paper. In this paper, we focus on the prediction of the tensile breaking strength, the most commonly used physical property for paper characterization. The model is based on the model developed by Shallhorn and Karnis, which was adapted to take into account the fiber morphological distributions. It was successfully applied in the absence of fiber breaks during the test and validated with the 10 pulps used in the first part of the study.

Application: The 3-D computational simulator of paper structure can be used to predict physical properties such as tensile strength to highlight the influence of morphological parameters of the fibers.

Investigations of relationships between the morphology of fibers and paper properties began in the early 1900s [1]. However, results have often been contradictory. One of the first fiber properties related to paper strength properties was fiber length. Several investigators found that fiber length directly affects the tensile strength of paper [2]. This led to the conclusion that hardwood pulps are lower in paper strength properties because the fibers of hardwoods are shorter than those of softwoods. However, contradicting evidence suggests that fiber length does not have a great influence on paper properties, especially on tensile strength, and that other factors influence tensile strength, including morphological properties, fiber strength [3], effects of chemical or mechanical treatments in the pulping and papermaking process, quality of sheet formation, etc.

Tensile strength is the most commonly used physical property for paper characterization, and the most often studied. Published works on tensile strength can be divided into two categories: 1) experimental studies about the influence of morphological parameters, physical and chemical treatments, unit operations in the process such as beating [4], and use of additives such as cationic starch [5], and 2) physical modeling to understand the effect of some structural parameters [6,7].

We decided to focus only on morphological parameters as the basis for a tensile strength prediction module in our simulator, which must be suitable for industrial application, and so must give results in a short computing time with a standard computer.

MODEL SELECTION

To minimize computation time and memory capacity requirements, the simulator [8] generates small square samples measuring about 2.5 mm x 2.5 mm. This is sufficient to obtain repeatable density results and also to predict the tensile strength assuming this property is controlled by the microstructure, and not by macrodefects (although both concepts are supported in the literature) [9-11].

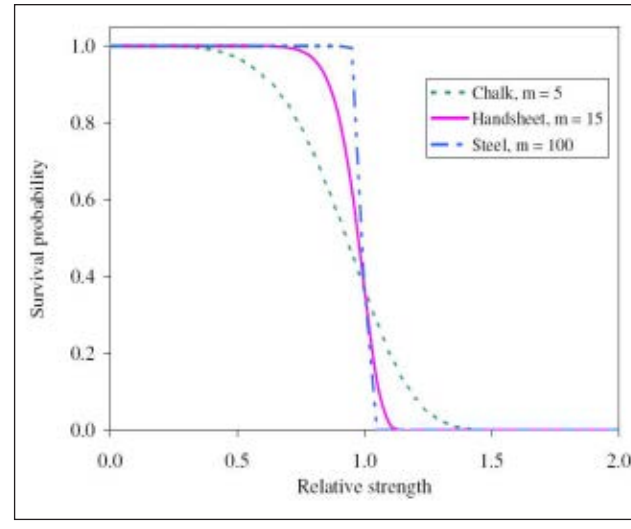

1. Comparison of the survival probability as a function of the relative strength for handsheets, chalk, and steel, displaying the influence of the Weibull modulus.

The Weibull modulus, which is a measure of the statistical scatter displayed by fracture events, can be used to determine which of the microstructure or macrodefects plays a major role on mechanical behavior. In general, nonhomogeneous materials have a modulus below 12, whereas homogeneous materials give values greater than 20. Chalk, for instance, is a brittle material; its Weibull modulus is around 5. Steel is generally a ductile material, with a Weibull modulus of about 100. **Figure 1** depicts the influence of the Weibull modulus on the survival probability to a fracture test (i.e., on the scatter of the results). It shows the strong difference in terms of mechanical behavior between steel and chalk. To

determine in which category to classify our handsheet samples, we performed tensile tests and assessed the Weibull modulus value. We obtained an average value of 15 for the different pulps used, which is in between the limits separating nonhomogeneous and homogeneous materials. However, the Weibull modulus does not have a linear effect on mechanical behavior and, with a value of about 15, we can consider paper as an homogenous material: its mechanical behavior is mainly controlled by its microstructure.

Sample size also might be an important parameter. Silvy [9] et al. showed that the average value of tensile strength could decrease by about 20% when the sample length was increased from 3 cm to 75 cm, through the influence of the macrodefects. But other factors, such as the fiber morphology and beating, have a prevailing influence. Thus, the development of a model based on structure only is acceptable and should bring to fore the causes of the main variations.

Various semiempirical or theoretical approaches for predicting the tensile strength of planar fibrous networks have been published [6,7]. From a theoretical point of view, one question should be answered: how does the transfer of stress between fiber segments take place? One should know whether the interfiber bonds are equally loaded or if the classic shear-lag theory applies. The purpose for this study, however, was to include a rapid prediction of the tensile strength of handsheets, using or adapting a model from the literature. Moreover, the study only concerns unbeaten bleached kraft pulps. Therefore, the strength of the interfiber bonds is relatively weak and almost no fiber breaks during the test. This is why we based our model on the model developed by Shallorn and Karnis [12].

DEVELOPMENT OF THE TENSILE STRENGTH MODEL

Shallorn and Karnis [12] developed a model based on the same concepts as Page [13]. The authors consider that the tensile strength of paper is a function of structural parameters such as fiber length, interfiber bonding strength, and fiber strength. In their model:

- paper is considered to be a continuous medium,
- each fiber is directly or indirectly entangled with the other fibers,
- all fibers are identical (same length and same diameter),
- all fibers are perpendicular to the fracture line, and
- fibers and interfiber bonds contribute to paper strength.

The model also assumes that all fiber bonds are equally loaded.

Considering a fiber embedded in a matrix of identical fibers, the force required to pull the fiber out of the matrix (T_f) is given by equation (1) where r is the radius of the fiber, x the embedded length, and τ the effective shear strength per unit fiber surface area.

$$T_f = 2 \cdot \pi \cdot r \cdot x \cdot \tau \tag{1}$$

Assuming a uniform distribution of the fibers perpendicular to the fracture, the tensile strength along the fracture line is given by equation (2), where N is the number of fibers that cross the fracture line per unit length, and L the fiber length.

$$T = \int_0^{L/2} \left(\frac{N}{L/2} \right) \cdot \left(2 \cdot \pi \cdot r \cdot x \cdot \tau \right) \cdot dx$$
$$T = N \cdot \pi \cdot r \cdot \frac{L}{2} \cdot \tau = N \cdot \left(2 \cdot \pi \cdot r \right) \cdot \frac{L}{4} \cdot \tau \tag{2}$$

In this equation, $(2 \cdot \pi \cdot r)$ is the perimeter of a cylindrical fiber and $L/4$ is the average length that is pulled out of the matrix.

This model was extended by several authors to include variable fiber orientation, fiber length distribution, dependence of coarseness on fiber length, and weak points [14]. Using the same concepts, we modified the equations proposed by Shallhorn and Karnis to account for the properties of the fibers and the network. The mathematical expression derived by Shallhorn for a single fiber becomes equation (3), where A_f is the surface area of the fiber that is released and τ_f is the shear strength of the bonds per unit surface area.

$$T_f = A_f \cdot \tau_f \tag{3}$$

This equation also can be written as follows:

$$T_f = P_f \cdot RBA_f \cdot x \cdot \tau_f \tag{4}$$

where P_f is the perimeter of the fiber and the relative bonded area (RBA_f).

The tensile strength of the sample is the sum of individual values:

$$T = \sum T_f = \left(\sum P_f \cdot RBA_f \cdot x \right) \tau_f \tag{5}$$

Thus, to predict the value of the tensile strength, we need to assess the value of the bonded area of each fiber that crosses the fracture line. This requires computing the values of the perimeter (P_f), the embedded length that is pulled out of the network, and the relative bonded area of the fiber. The position of the fracture line is chosen during the generation of the virtual network. Then, when a fiber crosses this fracture line, it is geometrically split into two pieces by this line. We assign the value of length of the shortest piece to x, because the shearing force is proportional to the length for a given fiber. Because the fibers are deposited one by one on the underlying network in the network generation process, we cannot compute the relative bonded area of each individual fiber. Therefore, we take into account the mean value of the RBA and the expression for the tensile strength becomes:

$$T = \left(\sum P_f \cdot x \right) RBA \cdot \tau_f \tag{6}$$

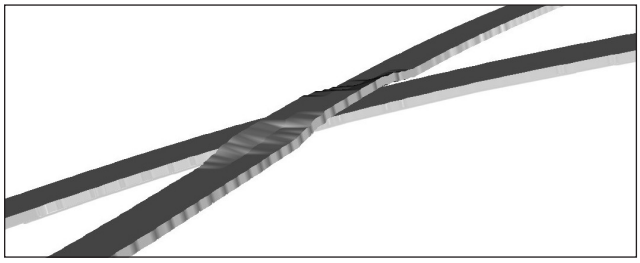

2. View of a fiber conformed on another one.

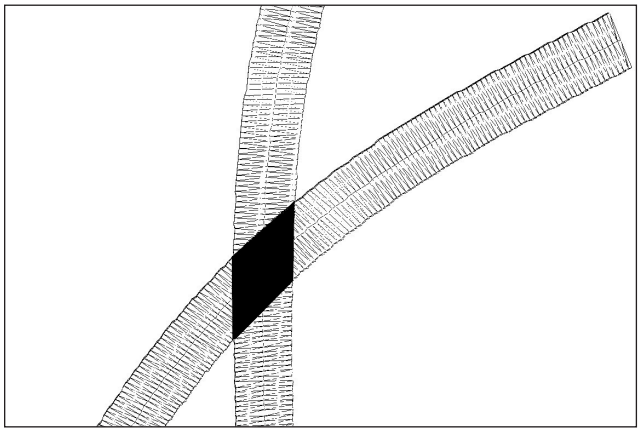

3. View of the actual bonded area.

A general relationship should take into account the orientation of the fibers in the network with respect to the tensile direction [15]. Because we are considering isotropic sheets, this simplification is appropriate. Finally, we also must assess bonding strength.

VALUE OF THE RELATIVE BONDED AREA

By definition, the relative bonded area is the ratio between the cumulative bonded area and the cumulative area of the fibers. When a new fiber is generated, deposited, and conformed on the underlying network, the program computes the position of the contact points with the underlying surface. Because of the dense meshing of the fibers, if we know the value of the surface area covered by a contact point (approximately 30 μm²), we can assess the value of the contact area. **Figure 2**, for instance, depicts one fiber conformed on another. **Figures 3** and **4**, respectively, show the actual contact area (1325 μm²) and the computed area (1340 μm²), with a difference of only 1.1%. In general, the error due to the method is negligible, especially because we have considered one of the most critical cases. Indeed, when the fibers are perpendicular or parallel, the error is nearly zero. Thus, knowing the cumulative contact area and the total surface area of the fibers, we can assess the average value of the relative bonded area.

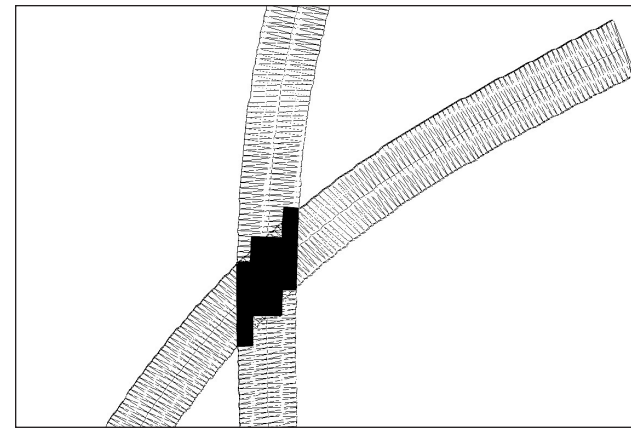

4. View of the computed bonded area.

RESULTS AND DISCUSSION

In a previous paper [8], we presented the main features of the simulator and the validation of a global structure property, namely the apparent density. To validate the tensile strength model, we performed tensile tests [16] with handsheets prepared with the 10 pulps previously used (four from hardwoods and six from softwoods), ran simulations, and compared the results. For ease of reading, **Table I** presents the main morphological properties of these pulps. In this table, the values between brackets are the standard deviations of the fiber width and thickness distributions. The two columns on the right are the density and RBA values assessed by the simulator. Despite the morphological differences of the fibers, the apparent density of the handsheets and virtual networks varies in a very narrow range only [8]. This also is the case for

	°SR	Length μm	Width μm		Fiber thickness μm		Density g/cm³	RBA
Hardwood pulps								
Acacia	15	737	17.5	(4.2)	4.1	(0.8)	0.51	0.41
Eucalypt	13	783	19.1	(4.2)	4.5	(1.6)	0.49	0.40
Oak and chestnut	14	709	20.4	(4.5)	4.7	(1.5)	0.49	0.42
Poplar	17	766	22.8	(5.2)	4.6	(1.6)	0.51	0.40
Softwood pulps								
Mix A	15	1868	37.8	(11.3)	5.9	(2.2)	0.48	0.36
Mix B	14	1925	33.6	(9.2)	4.6	(1.6)	0.54	0.39
Radiata pine	12	2214	34.5	(12.8)	7.1	(2.5)	0.44	0.34
Red cedar	15	2003	35.2	(9.2)	4.7	(1.6)	0.53	0.38
Southern pine	15	2056	37.9	(11.5)	6.5	(2.4)	0.46	0.35
Spruce	15	1558	35.0	(8.8)	4.7	(2.0)	0.54	0.38

I. Pulp properties, density, and computed relative bonded area (RBA) of the virtual networks.

the computed RBA, with slightly higher values for the hardwoods than the softwoods.

The validation of the tensile strength simulation also will validate the microstructure generated by the simulator. To compute the tensile strength, the value of the strength of the interfiber bonds (τ_f) must be chosen. To fit the experimental results, only two values of τ_f were used, one for the hardwood pulps and one for the softwood pulps. It differs from the method used by Shallhorn and Karnis [12], who assigned a specific value for each pulp. In our study, we found that 0.94 N/mm² for the hardwoods and 0.71 N/mm² for the softwoods enabled us to best fit the experimental results.

Figure 5 shows the comparison between the experimental and predicted results for the ten pulps used. In this figure, the error bars are, on the one hand, the standard deviation of the measurements and, on the other hand, the repeatability error of the simulation results. The figure demonstrates very good agreement between the experimental and predicted values. **Figure 6** displays the global comparison of the results. It clearly shows the good correlation between the measurements and the predictions, with a coefficient of determination (r^2) equal to 0.987.

The predictions are slightly better for the softwood pulps than for hardwood ones. This might be because of the greater morphological complexity of the hardwoods and greater amount of fines. Another explanation is the smaller range of variation of the tensile strength for the hardwoods and the smaller range of variation of the morphological properties, compared with softwoods. Nevertheless, with only two values of the strength of the interfiber bonds, we are able to predict the value of the tensile strength of the handsheets.

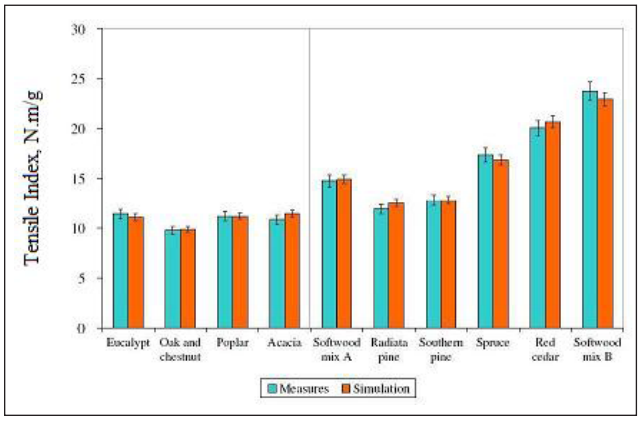

5. Comparison between the measured and predicted values for the tensile index.

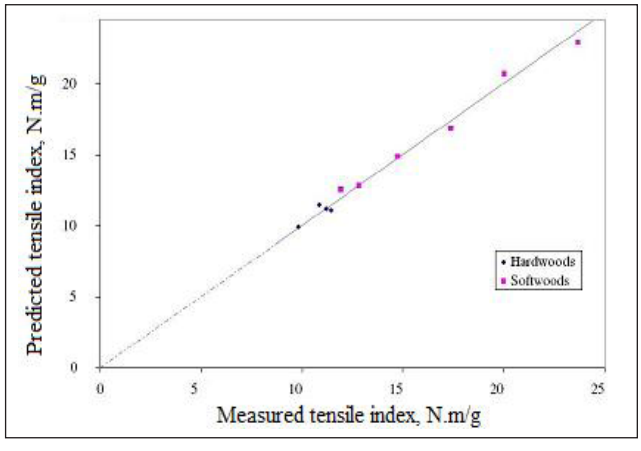

6. Correlation between experimental and predicted results for the tensile index.

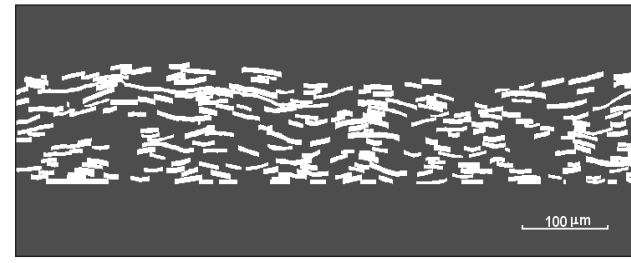

7. Cross-section of a virtual handsheet made of acacia pulp (60 g/m²).

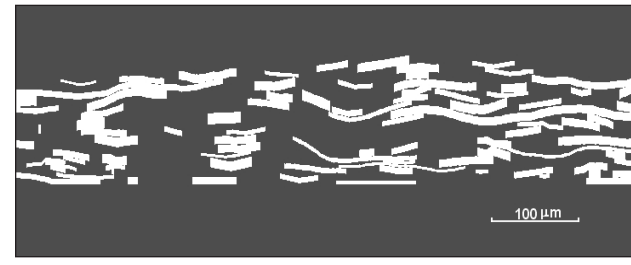

8. Cross-section of a virtual handsheet made of radiata pine pulp (60 g/m²).

The tensile index of unbeaten chemical pulps depends on the fiber length, but fiber length is not the only influencing morphological parameter. Figure 5 shows that the handsheets prepared with either radiata pine or southern pine pulps have tensile index values of the same order of magnitude as the hardwood pulps, despite their much greater fiber lengths (Table I). Compared with red cedar pulp, which has similar fiber length, the strength of the handsheets is divided by a factor of approximately two. This result is not surprising; radiata pine and southern pine pulps are well known for giving poor tensile index values because they have thick fiber walls. Therefore, the number of fibers that cross the failure line is significantly reduced compared to the other softwoods. Another factor is the decrease of the RBA value (Table I), resulting from the greater stiffness of the thick wall fibers. Nevertheless, it is less important than the number of fibers because the range of variation is reduced. With the same force required to pull out a single fiber, decreasing the total number of fibers that are pulled out of the network leads to a strong reduction of the global strength of the material. In the comparison with hardwoods, the increase of the number of fibers that cross the failure line (**Figs. 7** and **8**) partly compensates for the very short fiber lengths. For instance, the number of fibers that are pulled out is four times greater for acacia pulp than for radiata pine pulp.

Thus, considering the main differences between these fibers, we are able to show the dependence of the tensile

index on the morphology of the fibers. What is more important is the good agreement between experimental and predicted values, which also validates the microstructure generated by the simulator, which is taken into account here thanks to the relative bonded area.

CONCLUSION

Tensile strength is the most commonly used physical property for paper characterization, and the property most often studied. To predict the value of the tensile strength of handsheets made of unbeaten bleached chemical pulps, we implemented a simple model, adapted from the model developed by Shallhorn and Karnis, in our 3-D computational simulator. This model assumes that the fibers do not break during a tensile test. It takes into account the morphological properties of the fibers, which intervene in the computation of the length of the fibers that is pulled out and the relative bonded area. It also uses an adaptive parameter, which represents the interfiber bond strength. However, only two values of the bond strength were necessary to fit the experimental results, one for the hardwoods and one for the softwoods. This is possibly because of the type of pulps used. Moreover, with the good agreement found between the experimental and predicted values, we have another method to validate the microstructure of the network generated by the computational simulator and, in particular, the bonded area. **TJ**

ACKNOWLEDGEMENT

This research was supported by Ecole Française de Papeterie et des Industries Graphiques (EFPG), TEMBEC S.A., and Association Nationale de la Recherche et de la Technologie (ANRT).

LITERATURE CITED

1. Horn, R., "Morphology of wood pulp fiber from softwoods and influence on paper strength," U.S. Department of Agriculture Forest Service Research Paper, FPL 242, 1974.
2. Watson, A.J. and Dadswell, H.E., *Appita J.* 14(5): 168(1961).
3. Van den Akker, J.A., Lathrop, A.L, Voelker, M.H., et al., *Tappi* 41(8): 416(1958).
4. Niskanen, K., Ed., *Paper Physics*, Fapet Oy, Jyvaskyla, Finland, 1998.
5. Gailolas, C., Costa, A.P., Santos S.M., et al., *Appita J.* 57(2): 112(2004).
6. Jayaraman, K. and Kortschot, M.T., *Nordic Pulp Paper Res. J.* 13(3): 233(1998).
7. I'Anson, S.J. and Sampson, W.W., *Compos. Sci. Technol.* 67(7): 1650(2007).
8. Vincent, R., Rueff, M., and Voillot, C., *TAPPI J.* 8(9): 10(2009).
9. Silvy, J., Couty, D., and Arcondara. E., *Revue ATIP* 45(3): 115(1991).
10. Korteoja, M., Salminen, L.I., Niskanen, K.J., et al., *Mater. Sci. Eng.* A240: 173(1998).
11. Alkhasawneh, H. and Cameron, J.H., *Transactions of the 13th Fundamental Research Symposium*, Pulp And Paper Fundamental Research Committee, Bury, United Kingdom, 2005, p. 563–589.
12. Shallhorn, P. and Karnis, A., *Pulp Paper Mag. Can.* 80(12): TR92(1979).
13. Page, D.H., *Tappi* 52(4): 674(1969).
14. Johnston, R.E., *Appita J.* 50(5): 400(1997).
15. Jayaraman, K. and Kortschot, M.T., *J. Mat. Sci.* 31(8): 2059(1996).
16. NF EN ISO 1924-1 "Paper and board - determination of tensile properties - part 1: constant rate of loading method."

INSIGHTS FROM THE AUTHORS

Many fibrous resources are available for the paper industry and fiber morphology has a great influence on the structure of the end-products and their properties. Conventional methods for evaluating the papermaking potential of a pulp or pulp mix, or for optimizing a fibrous composition, require manufacturing laboratory samples and then performing physical testing. Although not a complete substitute for experimental work, computational simulation might serve as a rapid method for assessing properties, allowing for more selective experimentation.

Investigations of fibrous network structures seek a better understanding of the process mechanisms or the effect of raw materials on these structures and their physical properties. Many studies have been carried out, for many years, on this subject.

Our objective was to develop a simple 3-D computational model that could be used to visualize the structure and to predict physical properties, taking into account the real heterogeneity of the fibers in a paper sheet. One specification was to be able to run the simulations on a personal computer and get results in a short period. All the development stages were validated through experimental work.

The research presented several difficult aspects and challenges; accurately characterizing the 3-D morphology of the fibers, for example, was not an easy task. But, the most difficult aspect was certainly to develop a model that describes fiber arrangement and deflection in the structure.

It was interesting to find that the same model, with the same values of coefficients, enabled us to predict some macroscopic physical properties of handsheets for the tested pulps, which represented a very large panel of fiber morphologies.

Our next step is to include the effect of refining or chemicals, simulate fiber orientation to be closer to the case of real papers, and to predict other properties.

Vincent

Rueff

Voillot

Vincent was a PhD student at Laboratoire de Génie des Procédés Papetiers (Grenoble INP) and was working for Tembec S.A. Saint Gaudens during his doctoral studies. Rueff and Voillot are professors at Ecole Internationale du papier, de la communication imprimée et des biomatériaux (Grenoble INP - Pagora). Email Martine.Rueff@grenoble-inp.fr.

Characterizing carbonaceous biochemical oxygen demand load reductions from pulp and paper mills for activities related to total maximum daily loads

JAMES E. PALUMBO AND LINFIELD C. BROWN

ABSTRACT: Characterizing the effect of organic materials on receiving water-dissolved oxygen levels is important in water quality assessment studies involving pulp and paper facilities. Long-term biochemical oxygen demand (LTBOD) tests of pulp and paper effluents can be used to estimate many important characteristics such as ultimate BOD, rate coefficients, ultimate to 5-day BOD ratios (f-ratios), and reactivity. However, many of these characteristics are difficult to forecast as a function of future efforts to improve wastewater treatment, which is precisely what is needed for typical water quality assessments such as total maximum daily loads (TMDL). We provide a conceptual framework using simulation to predict effluent BOD characteristics as a function of improved wastewater treatment. The simulations use equations that describe BOD kinetics and are able to reproduce trends in f-ratio observed at various pulp and paper facilities and predict BOD reactivity as a function of treatment.

Application: Mills can use the methods we described to predict effluent characteristics as a function of future wastewater treatment improvements.

In the United States, low dissolved oxygen (DO) is one of the leading causes of water quality impairment [1]. Approximately 70 pulp and paper mills are located upstream of DO-impaired waters and 19 mills are located in the immediate vicinity of impaired waters [2]. While proximity does not indicate causation, the location of these pulp and paper mills suggests that a sizable portion of the industry may become involved in total maximum daily load (TMDL) or waste load allocation (WLA) assessments to assure that DO standards are being met. Such assessments are typically made using water quality models that relate discharges of organic matter to the DO response of the particular receiving water.

A critical aspect of a water quality model assessment is the characterization of the organic matter discharged into the receiving waters. Traditionally, water quality models have relied upon carbonaceous biochemical oxygen demand (CBOD) as a surrogate for organic matter, with CBOD characteristics estimated using long-term biochemical oxygen demand (LTBOD) testing [3]. The results of this test can be used to quantify the total amount of reactive organic matter in the sample and to estimate oxidation rate coefficients. A useful result of CBOD testing is the ratio of ultimate CBOD to 5-day BOD (i.e., the f-ratio), which allows the frequently performed 5-day BOD measurement (BOD_5) to be translated to ultimate CBOD ($CBOD_u$) that is necessary for the water quality model. Another useful result is the estimation of fast- and slow-reacting CBOD fractions that characterize the heterogeneous mixture of compounds with varying reactivity found in many pulp and paper effluents. Many modern water quality models feature multiple inputs to account for the varying reactivity of CBOD [4–6].

The typical water quality modeling cycle contains several phases including model selection, calibration, confirmation, and forecasting [7]. During calibration and validation, the modeler uses the available data to ensure that the model can represent existing DO conditions. When forecasting, the modeler attempts to predict DO concentrations under assumed future conditions. In TMDL and WLA scenarios, future conditions may include source load reductions of CBOD, implying that the discharger will perform some action to reduce loads. However, beyond knowing what the approximate target decrease in CBOD load may be, there is little direct information to guide the modeler in characterizing the future f-ratio and the slow and fast CBOD fractions as a function of the actions taken to reduce load. This lack of information can cause significant uncertainty in forecasting the response of DO to changes in CBOD load. Our goal was to provide a conceptual framework for the trends that have been observed between effluent BOD_5 and the f-ratio based upon the analysis techniques developed for LTBOD studies. We developed this framework through simulation procedures and extended it to include the partitioning of total CBOD into slow and fast fractions. The results of our work can be used to inform receiving water quality modeling studies, thereby providing needed guidance on the effect of load reductions on pulp and paper effluent CBOD characteristics.

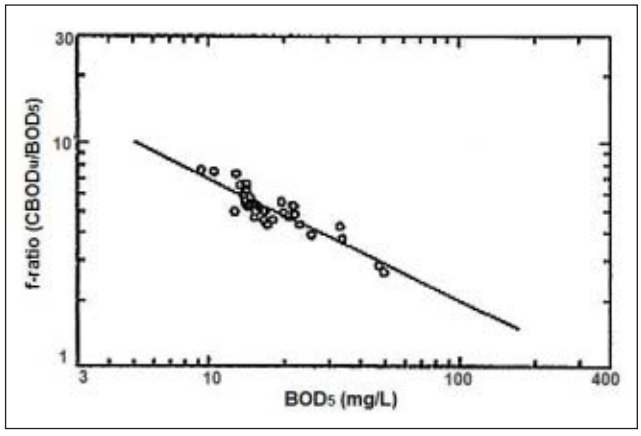

1. Variation of the f-ratio as a function of BOD_5 at a single mill (Mill A).

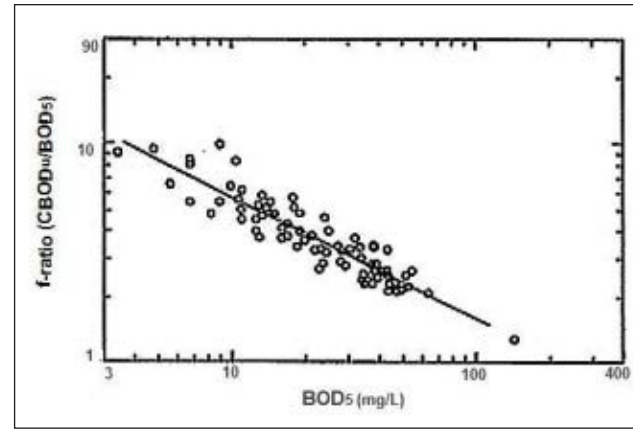

2. Variation of f-ratio as a function of BOD_5 at several mills.

BACKGROUND

Indirect information that provides insight into how f-ratios change under reduced loads originates from pulp and paper facilities that perform multiple LTBOD tests during the year; this takes the form of observed f-ratios as a function of effluent BOD_5 results. **Figure 1** shows a log space plot showing effluent variability of the f-ratio versus BOD_5 for an integrated bleached kraft mill using an activated sludge waste water treatment process [8]. There is a clear trend of increasing f-ratio with decreasing BOD_5 at this particular mill. **Figure 2** presents a compilation of effluent results at multiple pulp and paper facilities using bleached kraft, unbleached kraft, and mechanical pulping processes with activated sludge and aerated stabilization basin wastewater treatment [8]. Figure 2 indicates that the trend observed at an individual mill can also be observed over a broader range of effluents from facilities employing a variety of pulping processes and waste water treatment technologies.

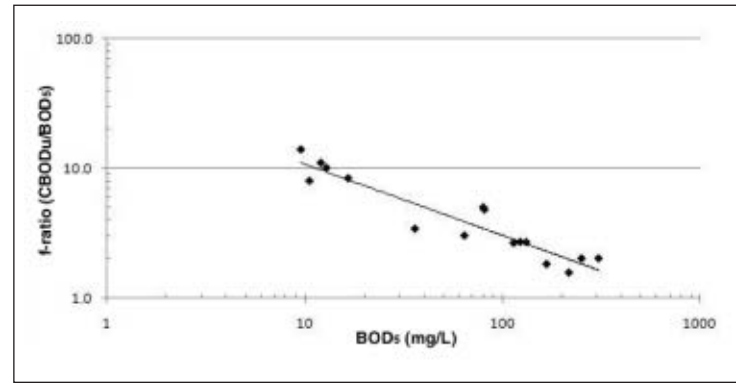

3. Variation of f-ratio as a function of BOD_5 for different processes and treatment levels.

Figure 3 presents f-ratios as a function of BOD_5 obtained from laboratory studies [9]. Primary effluents, final effluents, and final effluents subjected to solids removal were included, and the samples were taken from multiple facilities representing a wide range of pulping and wastewater treatment processes.

The data in Figs. 1–3 show that as BOD_5 decreases the f-ratio increases. This increase in f-ratio can be empirically described with a power function of the form in equation (1):

$$Y = \alpha X^{\beta} \quad (1)$$

Where:
Y = $CBOD_u/BOD_5$
X = BOD_5
α= coefficient
β= coefficient

The equation is linear in log space:

$$\log Y = \log\alpha + \beta \log X \quad (2)$$

Site	α	β
Mill A[1]	31.6	-0.63
Mill B[1]	16.3	-0.41
Mill C[1]	24.1	-0.54
Mill D[1]	12.1	-0.44
Various mills[1]	20.3	-0.55
Various mills, various levels of treatment[2]	38.4	-0.55

1. (8)
2. (9)

I. Summary of power function parameters from several data sources.

Table I summarizes the parameters of the power function fit to several datasets including effluent samples from individual facilities, a combined dataset of effluent samples from various mills, and a dataset from laboratory studies of various mills and treatment levels.

On the basis of the data in Figs. 1–3, which represent multiple facilities, papermaking processes, and treatment levels,

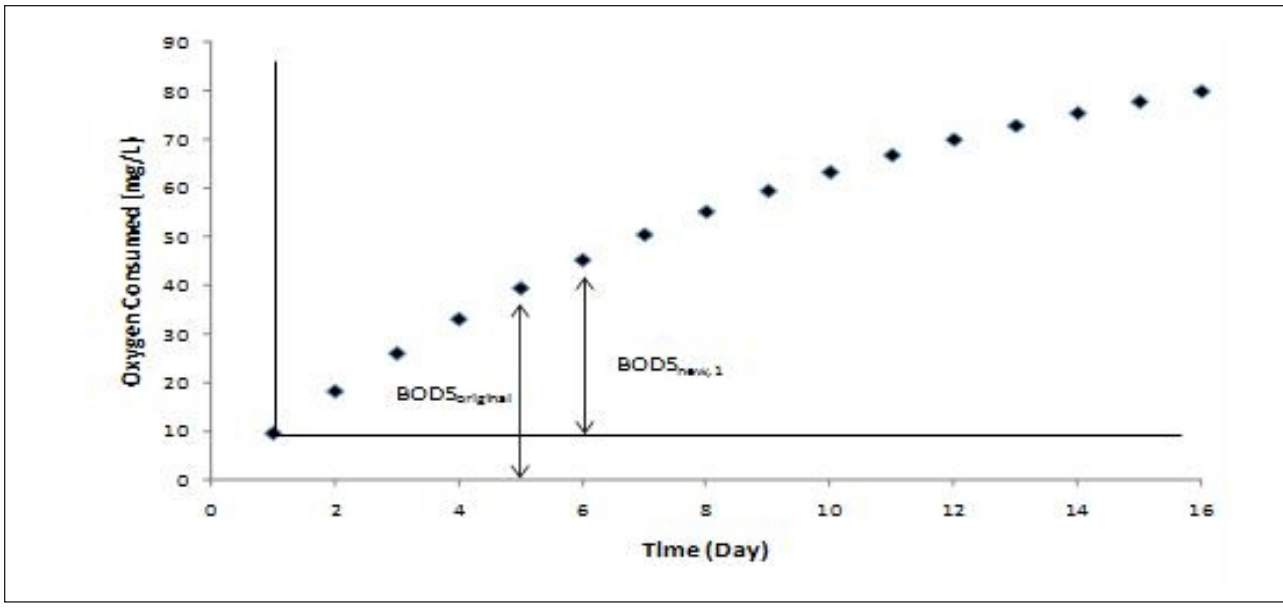

4. Long-term BOD time series generated with k = 0.1 day^{-1} and L = 100 mg/L. The inner axes and arrow show the BOD_5 of the new series when the origin is shifted to the value of the data point at day 1.

it can be reasonably concluded that the f-ratio of a pulp and paper effluent increases as BOD_5 is reduced. This increase generally follows a power function; however, the data from several mills shows variability in the parameters that characterize the power function.

While these observed trends and the associated fitted equations are insightful, it would be premature to conclude that they are representative of f-ratio behavior in all circumstances. In addition, the reported data characterize only the behavior of the f-ratios. Insight regarding the slow and fast fraction of effluent CBOD cannot be gained from the available data that are available. Broader understanding is necessary to characterize the effect of future load reductions on CBOD characteristics. The following simulation results illustrate a conceptual framework based on LTBOD equations that can explain observed f-ratio behavior in pulp and paper wastewaters and can be extended to characterize slow and fast CBOD fractions.

SIMULATION

Typically, CBOD characteristics from wastewater are calculated from the results of a LTBOD test. Various kinetic models that describe the oxygen consumption in terms of rate coefficients and ultimate oxygen demand are then fit to these data. A well-known and commonly used kinetic model is the first order decay model in equation (3).

$$BOD(t) = L(1 - e^{-kt}) \quad (3)$$

Where:
BOD(t) = BOD exerted at time = t
L = Ultimate BOD (mg/L)
k = first order rate coefficient
t = time

To understand the effect of BOD_5 reduction on the f- ratio, a simple simulation experiment using the first order model can be performed. **Figure 4** presents a theoretical time series of CBOD data from an LTBOD test on a pulp and paper wastewater. The time series consists of oxygen consumed versus time at one day intervals. In Fig. 4, the data are generated from a first order model as in equation (3), with k = 0.1 day^{-1} and L = 100 mg/L. The BOD_5 is equal to the oxygen consumed after 5 days (indicated in the figure as $BOD5_{original}$), and $CBOD_u$ = L.

The location of the origin can be shifted to coincide with the data point at day 1 to form a new time series starting at t = 1 day. This new series is what would be obtained if the original wastewater were given additional treatment prior to performing the LTBOD test, resulting in a reduced effluent load. In other words, additional treatment is equivalent to starting the BOD time series later. It is assumed that the progression of oxygen demand versus time would be the same as with the original sample. The new BOD_5 and $CBOD_u$ will be lower than with the original time series, but the rate coefficient is the same. In this case, the BOD_5 and $CBOD_u$ of the new (shortened by 1 day) series can be computed from the values in the original complete series as follows in equation (4).

$$\begin{aligned} CBODu_{new,1} &= CBODu_{orig} - BOD(1)_{orig} \\ BOD5_{new,1} &= BOD(6)_{orig} - BOD(1)_{orig} \end{aligned} \quad (4)$$

Where:
new, 1 = the values for the new series starting at day 1
orig = the values of the original series, starting at time zero

These relations can be generalized for any shift or start time, t, as follows in equation (5):

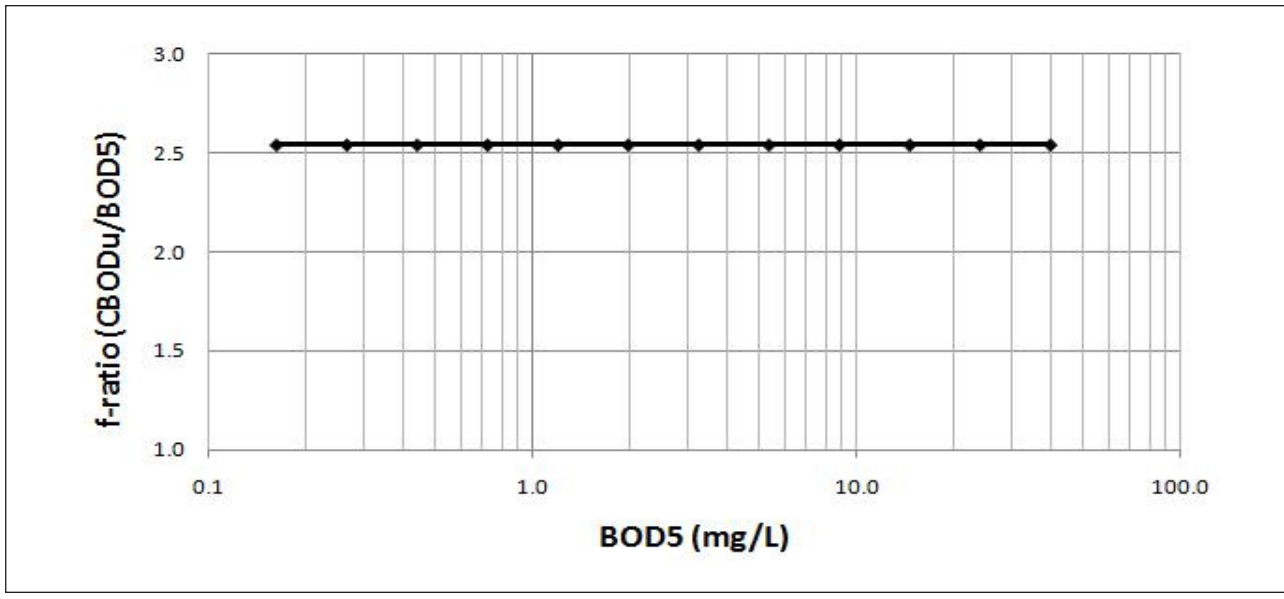

5. Results of f-ratio simulation using the first order model.

$$CBODu_{new,\,t} = CBODu_{orig} - BOD(t)_{orig}$$
$$BOD5_{new,\,t} = BOD(t+5)_{orig} - BOD(t)_{orig} \quad (5)$$

If the f-ratio $(CBOD_u/BOD_5)_{new,\,t}$ is computed for all values of t (i.e., for successive degrees of treatment) and plotted versus $BOD5_{new,\,t}$, then it can be observed how the f-ratio changes with BOD_5. **Figure 5** shows the plot for the simple first order time series in Fig. 4.

The results presented in Fig. 5 show that the f-ratio does not change as treatment increases if the wastewater CBOD follows first order kinetics. This result is produced due to the mathematical properties of the first order decay model. The solution for an f-ratio based on the first order model is shown in equation (6):

$$\frac{CBODu}{BOD5} = \frac{1}{1-e^{-5k}} \quad (6)$$

The equation demonstrates that the f-ratio calculated using the first order model is only a function of the rate coefficient and thus is invariant with regard to additional treatment. Deviation from the results forecast by equation (6) was demonstrated in Figs. 1–3, suggesting that the wastewaters from pulp and paper operations are not following first order kinetics.

Pulp and paper wastewaters do not follow first order kinetics because of the heterogeneous mixture of compounds with varying reactivity found in the wastewater. Several studies [10, 11] have found that dual first order kinetics, sometimes referred to as a sum of first order kinetics, fit pulp and paper wastewater significantly better than first order kinetics. The dual first order model estimates a fast and slow CBOD for the wastewater, as shown in equation (7).

$$CBOD(t) = L_1(1 - e^{-k_1 t}) + L_2(1 - e^{-k_2 t}) \quad (7)$$

Where:
L_1 = Fast ultimate CBOD (mg/L)
L_2 = Slow ultimate CBOD (mg/L)
k_1 = Fast rate coefficient (day^{-1})
k_2 = Slow rate coefficient (day^{-1})

A simulation similar to the one described for the first order model was developed for the dual first order model. Wastewater with the following characteristics was simulated and the $CBOD_u/BOD_5$ ratio recorded: $L_1 = 50$, $L_2 = 50$, $k_1 = 0.10$, $k_2 = 0.01$. **Figure 6** presents the results of the simulation. The simulation using the dual first order model resulted in an increase in the f-ratio as BOD_5 decreased and the overall trend of the increase was nearly linear in log space. This result was very similar to the data presented in Figs. 1–3 and indicates that the dual first order model is structurally able to simulate the trends identified in the data. Mathematically the f-ratio in the dual first order model is a function of the rate coefficients and the original amounts of slow and fast CBOD. This can be seen in the solution of the dual first order model for the f-ratio as presented in equation (8).

$$\frac{CBODu}{BOD5_{new,\,t}} = \frac{L_1 e^{-k_1 t} + L_2 e^{-k_2 t}}{L_1\left(e^{-k_1 t} - e^{-k_1(t+5)}\right) + L_2\left(e^{-k_2 t} - e^{-k_2(t+5)}\right)} \quad (8)$$

Where:
t = amount of additional treatment time

The dual first order model may provide insight into the underlying mechanism for the observed f-ratio trend. This model

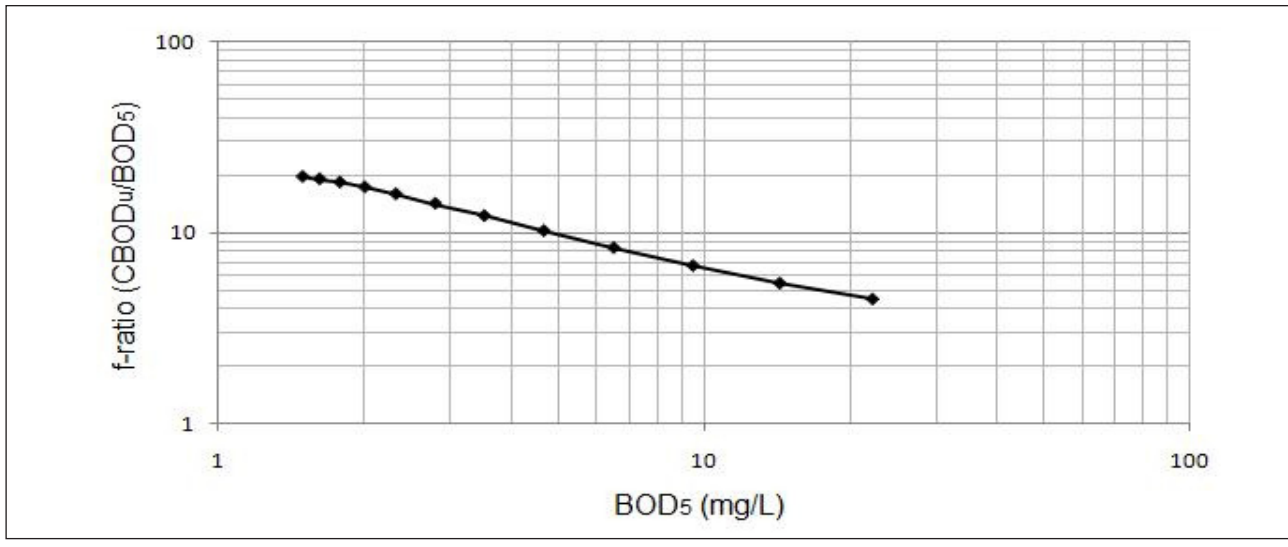

6. Results of $CBOD_u/BOD_5$ simulation using dual first order model.

CBOD	L	k	f-ratio
Fast	500	0.1	2.5
Slow	50	0.01	20.5

II. Hypothetical wastewater characteristics.

postulates that one fraction of CBOD is removed at a faster rate than another fraction as BOD_5 decreases due to treatment. This change in proportion of fast to slow CBOD alters the right side of equation (8) for every incremental step of BOD_5 removal; therefore, the f-ratio varies as a function of treatment in this model in contrast to the first order model.

Table II summarizes the initial conditions of a hypothetical wastewater simulated with equation (8) over a large range of BOD_5 values, representing varying levels of treatment. Table II includes the ultimate fast and slow CBOD concentrations, rate coefficients, and individual f-ratios for each fraction of the hypothetical CBOD. **Figure 7** shows the simulation results for the f-ratio using the dual first order model with the parameter values in Table II.

The simulation results in Fig. 7 show that when the remaining fast CBOD is much greater than the remaining slow CBOD at lower treatment levels, then the composite f-ratio of the wastewater most closely resembles the f-ratio of the fast CBOD. When the remaining slow CBOD is much greater than the remaining fast CBOD at high treatment levels, then the wastewater's f-ratio approaches the f-ratio of the slow CBOD. Most wastewaters likely lie in the transition area between

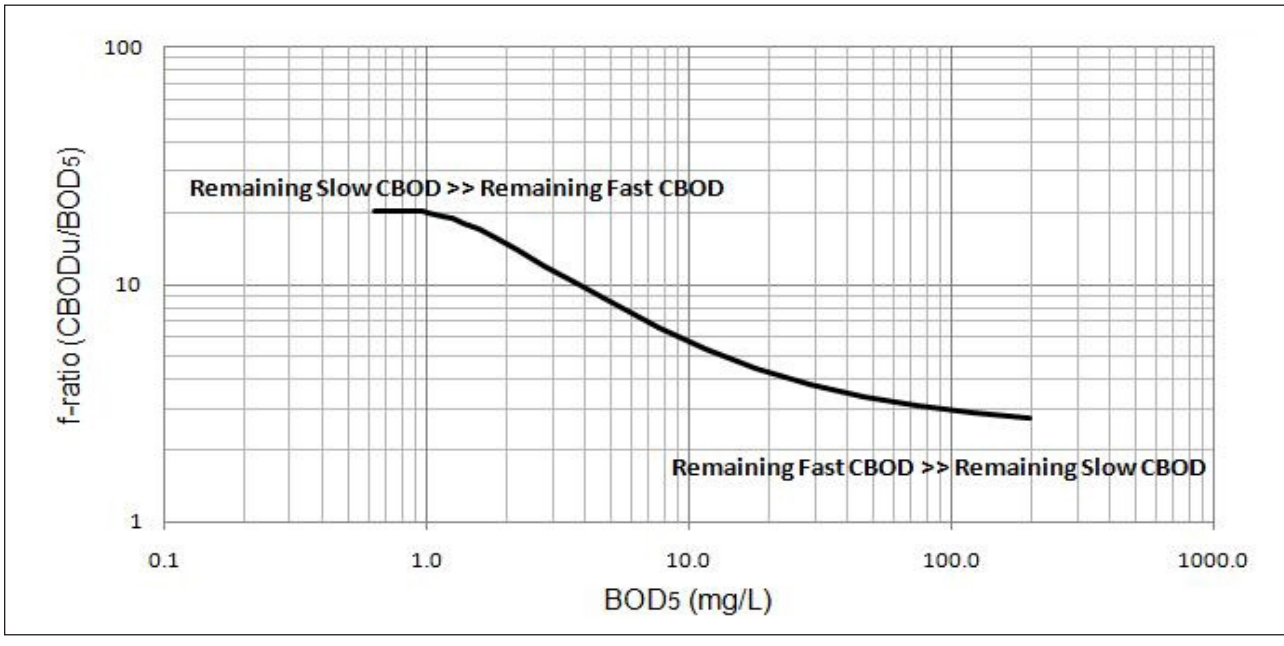

7. Simulation of f-ratio over extended treatment time for a hypothetical wastewater.

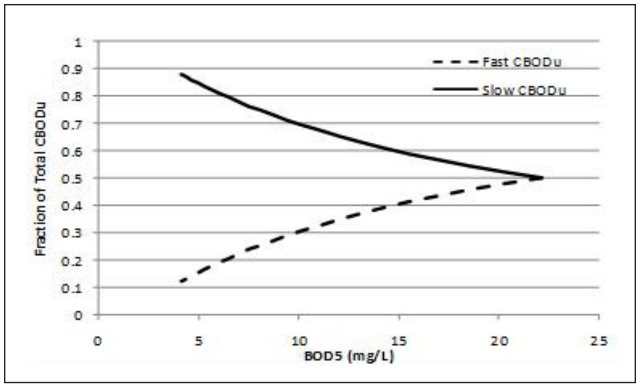

8. Slow and fast $CBOD_u$ fractions as a function of BOD_5 using dual first order model.

these two extremes. Therefore, the relationship between decreasing BOD_5 and increasing f-ratio that is observed in Figs. 1–3 is a snapshot of a sigmoidal behavior between two extremes. When treatment is increased or decreased and BOD_5 changes, the f-ratio responds positively.

DISCUSSION

Treatment effects on slow and fast $CBOD_u$ fractions

In addition to the f-ratio, many modern receiving water quality models have multiple inputs of CBOD based on reactivity. When BOD_5 loads are reduced due to additional treatment, the ratio of fast to slow CBOD also changes. So, when simulating treatment, both the f-ratio and the $CBOD_u$ fractions should be updated in the receiving water quality model. This concept can be demonstrated by example. **Figure 8** shows the fraction of $CBOD_u$ as slow and fast and as a function of BOD_5 for wastewater with the characteristics $L_1 = 50$, $L_2 = 50$, $k_1 = 0.10$, $k_2 = 0.01$.

As an effluent receives simulated additional treatment, the fraction of slow CBOD increases while the fast fraction decreases as expected because by definition, fast CBOD oxidizes faster than slow CBOD.

Limitations on the extent of fast CBOD removal

Equation 8 can generate f-ratios that are outside of the domain of industry experience for even highly treated wastewaters. The f-ratios plotted against BOD_5 in Figs. 1–3 rarely are above 9 for tests on secondary treated effluents, with most of the relatively high f-ratios residing in the 7–8 range. Other LTBOD studies on well-treated effluents [12] have agreed with this upper boundary. However, using equation (8), f-ratios can reach levels well over these values for BOD_5 concentrations that are low, but achievable. This suggests that the conceptual framework may break down above a certain treatment level.

One reason for this breakdown may be a limitation for how much fast $CBOD_u$ can actually be removed from a biological treatment system. The fast BOD in modern effluents is likely made up of a significant amount of cellular materials from microbial growth. Because new cells are synthesized to oxidize CBOD, but these cells represent CBOD themselves, it is unlikely that CBOD from cells could be completely removed from the effluent. A certain fraction of CBOD (which would be characterized as fast CBOD in a pulp and paper wastewater) may be continuously formed and thus be effectively untreatable in a typical secondary treatment system. A residual amount of fast CBOD that is invariant to treatment time may limit the applicability of equation (8) to f-ratios that are less than approximately 10.

Changes in f-ratio due to mill process changes

The treatment described up to this point is representative of improved $CBOD_u$ removal in the wastewater treatment plant. A mill may also have the option of reducing the load of BOD that is sent to wastewater treatment through in-mill process changes. This type of influent load reduction would likely result in a different effect on the f-ratio than improved CBOD removal. Simulations can be performed to understand this effect by varying the initial concentrations of slow and fast CBOD in equation (8). However, this is an area for future research as it is not clear how mill process changes might affect slow and fast CBOD concentrations.

Application to receiving water quality modeling studies

During the forecasting phase of a receiving water quality modeling study, various loading scenarios can be examined including daily maximum and monthly average loads from an individual pulp and paper point source and various load combinations among several sources. The concepts we presented can be useful in estimating appropriate f-ratios and fast and slow fractions for these and other forecasted loading scenarios. Application of the concept is appropriate only where the CBOD load reduction is due to improved wastewater treatment. It is not appropriate for other load reduction options such as influent load reductions due to process changes, solids removal, and land application. In addition, estimates of dual first order model parameters from site-specific LTBOD tests are necessary to define the relationships between treatment, f-ratio, and reactivity at each facility.

SUMMARY

Little information exists for predicting the future CBOD characteristics of a reduced load in a receiving water quality model. We developed a conceptual approach to provide general guidance to water quality modelers identifying the future f-ratios and reactivity of pulp and paper mill effluents. The approach uses the dual first order model to simulate the f-ratio behavior observed at a variety of pulp and paper mill facilities. The results of these simulations were very similar to observed f-ratio behavior at a variety of facilities, suggesting that an effluent's f-ratio changes as a function of the fast to slow CBOD ratio. As BOD_5 is reduced due to additional treatment, fast CBOD is preferentially removed, thus changing the proportion of fast to slow CBOD and increasing the

f-ratio. This interrelated nature of the f-ratio and dual first order model parameters can be shown mathematically and allows the concept to be extended to other aspects of CBOD characterization such as the fraction of slow and fast CBOD in the effluent after incremental BOD_5 removal. These results may prove useful for water quality modeling studies involving the effect of pulp and paper mill CBOD loads on dissolved oxygen in receiving waters. **TJ**

LITERATURE CITED

1. U. S. Environmental Protection Agency, *National Summary of State Information, Water Quality Assessment and Total Maximum Daily Loads Information (ATTAINS)*, Accessed September 15, 2009, from http://iaspub.epa.gov/waters10/attains_nation_cy.control#APRTMDLS.
2. National Council for Air and Stream Improvement Inc., *NCASI Receiving Water Database*, NCASI, Research Triangle Park, NC.
3. American Public Health Association, American Water Works Association, Water Environment Federation, *Standard Methods for the Examination of Water and Wastewater*, 20th Edn. American Public Health Association/American Water Works Association/Water Environment Federation, Washington, DC, 1998.
4. Wool, T. A., Ambrose, R. A., Martin, J. L., et al., *Water Analysis Simulation Program (WASP): Version 6.0 Users Manual*, United States Environmental Protection Agency, Athens, GA, 2003.
5. Brown, L. C., *QUAL2E Version 5.1 User Manual and Documentation*, Tufts University, Medford, MA, 2005.
6. Chapra, S. C., Pelletier, G. J., and Tao, H., *QUAL2K: A Modeling Framework for Simulating River and Stream Water Quality, Version 2.11: Documentation and Users Manual*, Tufts University, Medford, MA, 2008.
7. Chapra, S. C., *Surface Water Quality Modeling*, McGraw-Hill, New York, 1997.
8. HydroQual Inc., Unpublished data, Mahwah, NJ, 2009.
9. Martone, C. H., *Studies Related to the Determination of Biodegradability and Long Term Biochemical Oxygen Demand*, Master's thesis, Tufts University, Medford, MA, 1976.
10. McKeown, J. J., Brown, L.C., and Martone, C.H., *Water Science and Technology* 13(10): (1981)363.
11. National Council for Air and Stream Improvement, *A Review of Ultimate BOD Estimation and Its Kinetic Formulation for Pulp and Paper Mill Effluents*, NCASI Technical Bulletin 382, NCASI, Research Triangle Park, NC, 1982.
12. National Council for Air and Stream Improvement, Unpublished data, Research Triangle Park, NC, 2008.

INSIGHTS FROM THE AUTHORS

We were providing technical support to several mills involved in effluent receiving water quality activities and noticed that the characterization of future CBOD load reductions was problematic for many model based studies. In the absence of supporting information, most regulatory agencies apply conservative assumptions in order to be protective of the environment. Our goal was to provide information and a practical method to the industry for calculating realistic CBOD characteristics as a result of improved treatment.

While empirical relationships between CBOD characteristics and improved treatment have been previously noted, there is little information available that ties these observed relationships to a theoretical concept. The results of our research suggest a plausible explanation for the observed empirical relationships and provide a practical means for CBOD characteristics to be predicted in the absence of supporting data, which is the common situation.

The most difficult aspect of our research was identifying the practical boundaries of the simulation approach; for example, the upper limit of the calculated f-ratio. When taken to the extreme, our simulation calculates high f-ratio values for well-treated effluents. We compared our calculated values to various data sources and used basic wastewater theory to postulate why our simulation might break down for highly treated wastewaters.

The simulation was able to replicate the trends observed in the various datasets. That provided a great deal of insight into what might be occurring in these wastewaters and highlighted for us the utility of simulation approaches for solving problems.

Palumbo

Brown

This information may be useful to mills involved in water quality activities examining the impact of effluent organic materials on receiving water dissolved oxygen concentrations. We described methods that provide a realistic means of predicting effluent characteristics as a function of future treatment improvements. Some controlled experiments can provide further validation of the results. Future experiments can be designed to better understand the reasons for the apparent f-ratio upper boundary for well-treated wastewaters.

Palumbo is senior research engineer, National Council for Air and Stream Improvement, 600 Suffolk St., Lowell, MA 01854. Brown is professor emeritus, Department of Civil and Environmental Engineering, Tufts University, Medford, MA 02155. E-mail Palumbo at james_palumbo@uml.edu.

Calendering effects on coating pore structure and ink setting behavior

PETER RESCH, WOLFGANG BAUER, AND ULRICH HIRN

ABSTRACT: Coating layer pore structure significantly affects surface appearance, optical properties, and print-ability performance of multiply coated papers. Generally, fast ink setting can be realized by use of fine pigments, or pigments with steep particle size distribution. Ink-paper interaction of coated papers also changes significantly in calendering. The objective of this study was to better understand the influence of calendering on the pore structure of multilayered coated papers and to highlight the effect of this pore structure change on ink setting behavior. Laboratory calendering trials demonstrated that the pore structure of calendered paper is reduced with increased calendering temperatures. Mercury porosimetry and image analysis of scanning electron microscope images of calendered papers highlighted the gradual reduction of total pore volume, which, in combination with the reduced surface porosity, resulted in slower ink setting. If ink setting speed is to be preserved, calendering at low surface temperatures and a higher number of nip passes is preferred to reach a desired paper gloss level. Results also were compared to common theoretical models for liquid penetration into porous structures. These models can also be used to describe the influence of calendering-induced pore structure changes on ink setting. This work demonstrates optimization of calendering parameters to reach a balance for paper gloss and ink setting. The optimum depends on the machine equipment available and has to be checked separately for each concept of multiply coated paper and calender conditions.

Application: Results from this optimization study formed the basis for development of fast-drying offset printing grades with superior ink scuff resistance.

The pore structure of coated paper and its influence on ink setting and ink drying have received considerable interest. According to FOGRA (the German Graphic Technology Research Association), 35% of the problems in sheet-fed printing in 2006 were related to ink scuff, and 21% of the problems were related to ink setting and drying [1]. Such problems were emphasized because of shorter print runs, which, in combination with the economic pressure on printing houses, leads to less time between printing and converting of a paper.

As highlighted in previous publications [2,3], finer pigments result in a coating layer that contains finer pores. Nutbeem et al. showed that pore size is proportional to the product of particle size and steepness of size distribution for carbonate coatings [4]. The coating structure of the top coat is the dominating layer determining the interaction of the final multilayered coated paper with offset inks and paper gloss, as well as smoothness [5,6].

Calendering significantly changes the ink-paper interaction of coated papers. Through this study, we wanted to generate a better understanding regarding the influence of calendering on pore structure of multiple coated papers, and highlight the effect of pore structure changes on the ink setting behavior of the calendered paper. For this study we used triple-coated woodfree papers produced on a commercial paper machine and then calendered in the laboratory. Calender temperature, number of nip passes and line load were varied to find the optimum balance between competing performance properties such as paper gloss and set-off. The pore structure of the whole paper composite was analyzed with mercury porosimetry and surface porosity was assessed by evaluation of high-resolution scanning electron microscope (SEM) images (**Fig. 1**). Results were compared with the outcome from analytical models describing the effect of pore structure of coated papers on ink vehicle absorption.

THEORETIC CONSIDERATIONS

Surface porosity of porous substrates has to be taken into account in printing coated papers. By calculating the dimensionless void fraction, which is equivalent to the surface porosity as presented in equation (1), the linkage between the pore size (pore radius R) and the number of pores per unit area n_p can be performed:

$$surface\ porosity\ \varepsilon = n_p \cdot R^2 \cdot \pi \quad (1)$$

Porosity in the coating layer of coated papers is generated by pigment particles. Pore size and the number of pores is estimated from a theoretical particle packing model based on monodispersed, noninteracting spherical particles (simple cubic model) (**Fig. 2**).

When the monodisperse, spherical pigment particles with the corresponding particle radius $R_{pigment}$ are clustered (Fig. 2), surface porosity ε can be calculated analytically. It is defined as the ratio of pore area A_{void} to total area A_{total}.

$$Surface\ porosity\ \varepsilon = \frac{Pore\ \ Area}{Total\ \ Area} = \frac{A_{void}}{A_{total}} \quad (2)$$

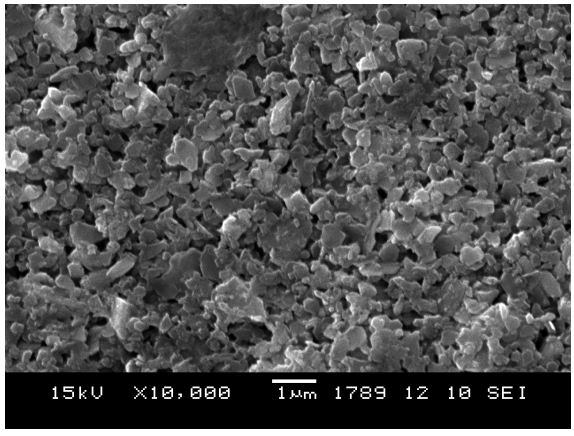

Uncalendered paper

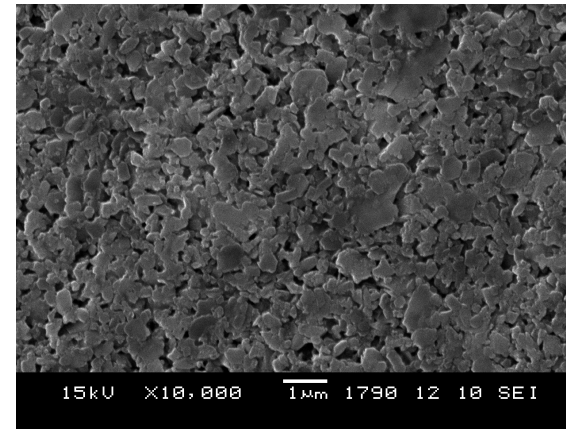

10 passes / 25°C / 30 N/mm

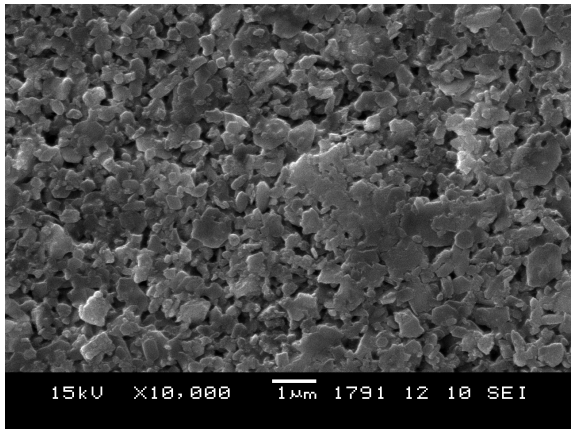

10 passes / 50°C / 30 N/mm

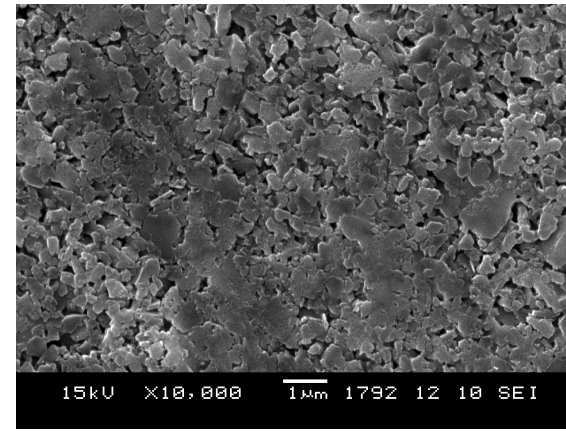

10 passes / 70°C / 30 N/mm

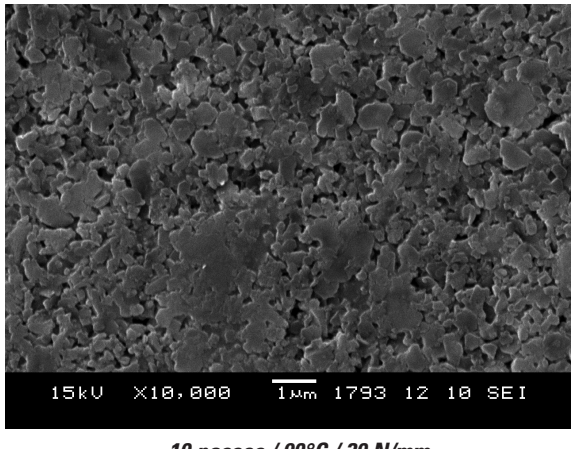

10 passes / 90°C / 30 N/mm

1. Scanning electron microscope (SEM) images of the laboratory calendered papers (nip passes / steel roll temperature / line load) at 10,000:1 magnification.

Pore area A_{void} is the difference between the total area A_{total} and the pigment area $A_{pigment}$, so $A_{void} = A_{total} - A_{pigment}$. Considering Fig. 2 for pigment area and total area (i.e., unit area), we obtain the following:

$$\varepsilon = \frac{A_{void}}{A_{total}} = \frac{A_{total} - A_{pigment}}{A_{total}} = 1 - \frac{4 \cdot R_{pigment}^2 \cdot \pi}{(4 \cdot R_{pigment})^2} = 1 - \frac{\pi}{4} \approx 0.215 = \text{constant} \quad (3)$$

In this case, surface porosity is constant and independent of pore size and, subsequently, independent of the pigment particle size. Although the example of an even spherical grid is hardly applicable for actual paper coatings, it illustrates a fundamental principle: changes in pigment size (given a constant steepness of the size distribution) do not affect surface porosity. This parameter is independent of the size of particles and is governed entirely by the geometry of the particular arrangement. Changes in pigment size affect the pore diameter, which influences liquid penetration.

PORE SIZE EFFECT ON FLUID PENETRATION

Various paper-related models have been used to describe the fluid penetration into pore structures. Initially, the Lucas-

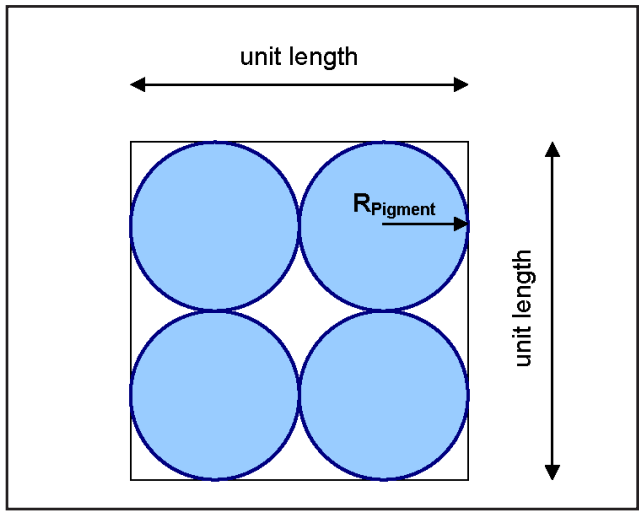

2. Particle packing of spherical pigments.

Washburn equation was used to describe the ink vehicle uptake by paper. Based on equation (4), the distance traveled by the liquid front in the tube is a function of the elapsed time, the fluid viscosity, the interfacial tension, and the contact angle between the fluid and the capillary pore radius as in equation (4):

$$x^2 = \frac{R \cdot \gamma \cdot \cos\theta \cdot t}{2 \cdot \eta} \tag{4}$$

Symbols used in this and later equations represent the following:

V_p	penetration volume [m³/m²]
ε	void fraction equivalent to surface porosity [m²/m²]
x	penetration depth [m]
ϕ_s	solid's volume fraction original fluid [-]
t	time [s]
ϕ_f	solid's volume fraction filter cake [-]
R	pore radius [m]
ρ	density [g/m³]
$R_{pigment}$	radius of pigment particle [m]
K	Darcy coefficient [m²]
n_p	number of pores per unit area [1/m²]
$A_{pigment}$	pigment area [m²]
η	viscosity [g/m/s]
A_{total}	total area [m²]
γ	interfacial tension [g/s²]
A_{void}	pore area [m²]
θ	contact angle [°]

Equation (5) shows that, based on the Lucas-Washburn equation, a large number of coarse pores gives the highest penetration volume and, consequently, fastest ink vehicle uptake.

$$V_p = n_p \cdot \pi \cdot R^2 \cdot \sqrt{\frac{R \cdot \gamma \cdot \cos\theta \cdot t}{2 \cdot \eta}} = \varepsilon \cdot \sqrt{\frac{R \cdot \gamma \cdot \cos\theta \cdot t}{2 \cdot \eta}} \tag{5}$$

For a given surface porosity ε (defined in equation (2) as the ratio of pore area to total area), ink setting is faster with larger pores.

Schölkopf [7] compared the penetration models of Lucas-Washburn and Bosanquet. The main drawback of the Lucas-Washburn approach is that it neglects inertia of the penetrating fluid. Bosanquet added the inertia associated with an accelerated fluid, based on the following force balance:

$$F_i + F_{vd} = F_p + F_w \tag{6}$$

F_w is the inertial force according to Newton's second law, and equals $d(mdx/dt)/dt$, where m is the mass of the fluid in the capillary ($=\pi R^2 \rho x$) and mdx/dt is the momentum, or inertia, of the fluid. F_{vd} is the force due to viscous drag and follows Poiseuille's law. F_p is the force acting by an external pressure p_e and F_w is the capillary force. When the terms are brought in their dynamic form, we obtain the following Bosanquet relation:

$$\frac{d}{dt}\left(\pi \cdot R^2 \cdot \rho \cdot x \frac{dx}{dt}\right) + 8 \cdot \pi \cdot \eta \cdot x \frac{dx}{dt} = p_e \cdot \pi \cdot R^2 + 2 \cdot \pi \cdot R \cdot \gamma \cdot \cos\theta \tag{7}$$

For the case that the starting point is zero and no external pressure is applied, the distance traveled by the liquid front in a tube can be calculated as follows:

$$x^2 = \frac{2 \cdot \gamma \cdot \cos\theta \cdot t^2}{R \cdot \rho} \qquad (t << 1, p_e = 0) \tag{8}$$

$$V_p = n_p \cdot \pi \cdot R^2 \cdot \sqrt{\frac{2 \cdot \gamma \cdot \cos\theta \cdot t^2}{R \cdot \rho}} = \varepsilon \cdot \sqrt{\frac{2 \cdot \gamma \cdot \cos\theta \cdot t^2}{R \cdot \rho}} \qquad (t << 1, p_e = 0) \tag{9}$$

Based on equation (8), small pores lead to faster liquid uptake in a single capillary. Schölkopf et al. [8] showed that this type of flow, called inertial flow, changes to Lucas-Washburn flow as time and distance increase. The inertial forces are only relevant in the initial phase of the liquid penetration, at t<<1. The smaller the pore radius, the faster the changeover to Lucas-Washburn flow will occur. When the penetration volume per pore is calculated in equation (9), coarse pores give higher penetration volume. At a constant surface porosity ε, however, small pores give higher liquid absorption.

Preston et al. [9,10] chose a practical approach to describe the role of pore density on ink setting on coated papers. They measured the ink tack development of ink printed onto coated papers with a wide range of pore structures to study ink setting rates. Pore size and pore volume of coated papers were analyzed by mercury porosimetry. Based on the assumption that all pores are cylindrical, the pore density per unit area could be calculated. Gathered data confirmed that the Lucas-Washburn model could not be used to describe the ink setting behavior of offset inks on coated papers. An empirical expres-

sion for the total volume of ink vehicle absorbed into the coating structure at a given time was given as:

$$V_p = n_p \cdot \pi \cdot \sqrt{\frac{R^3 \cdot \gamma \cdot \cos\theta \cdot t}{2 \cdot \eta}} \quad (10)$$

$$V_p = n_p \cdot \pi \cdot R^2 \cdot \sqrt{\frac{\gamma \cdot \cos\theta \cdot t}{2 \cdot R \cdot \eta}} = \varepsilon \cdot \sqrt{\frac{\gamma \cdot \cos\theta \cdot t}{2 \cdot R \cdot \eta}} \quad (11)$$

Equation 10 deviates from the simple capillary imbibition model of Lucas-Washburn by a factor 1/R. Based on equation 11, we can conclude that a large number of coarse pores give the highest penetration volume and consequently fastest ink setting, which is in agreement with the finding of Schölkopf. Additionally, the model presented by Preston shows that at constant surface porosity ε, higher liquid absorption is achieved with smaller pores.

Xiang et al. [11,12] published several papers describing a filter cake model. In their model, the ink pigment particles and resins are too large to penetrate the finer coating pores and are filtered out on the surface. Based on investigations analyzing the coating structure change after printing, they found that the gel layer was able to prevent penetration of pigments into coarse pores.

The total volume of ink vehicle absorbed into the coating structure per unit area was calculated as follows:

$$V_p = \varepsilon \cdot \sqrt{\frac{R \cdot t \cdot \gamma \cdot \cos\theta}{2 \cdot \eta \cdot \left(1 + \frac{\varepsilon^2 \cdot \phi_s \cdot R^2}{8 \cdot K \cdot \phi_f \cdot (1 - \phi_s)}\right)}} \quad (12)$$

In case of low resistance of the coating filter cake, or as the filter cake permeability $K \rightarrow \infty$, equation (12) is reduced to the Lucas-Washburn equation:

$$V_p = \varepsilon \cdot \sqrt{\frac{R \cdot \gamma \cdot \cos\theta \cdot t}{2 \cdot \eta}} \quad (13)$$

If K is small, which means that the filter cake resistance becomes important, equation (12) can be reduced to the following:

$$V_p = \sqrt{\frac{4 \cdot K \cdot t \cdot \gamma \cdot \phi_f \cdot (1 - \phi_s) \cdot \cos\theta}{R \cdot \eta \cdot \phi_s}} \quad (14)$$

Based on equation (14), the total volume of ink vehicle that was absorbed into the coating structure per unit area is a function of $1/R^{1/2}$. So the filter cake model, which takes the resistance of the formed filter cake into account, predicts faster ink setting with smaller pores in the coating structure.

In conclusion, all models – except for the simplistic Lucas-Washburn model – suggest that for faster ink setting a fine pigment should be chosen. Total capillary volume is independent from pigment size, it is governed by the particle distribution steepness.

The theoretical analysis describing surface porosity as a function of the pigment particle size is valid for uncalendered papers. We presume that calendering leads to alignment and compression of the initial pore coating structure. The goal of our investigation, then, was to analyze the influence of different calendering settings on the compression level of coated papers and ink setting.

PORE STRUCTURE CHANGES AND INK SETTING

Coated papers typically have a matte or silk surface appearance, the result of a small degree of particle alignment after coating application. Calendering is used as a final step to develop paper gloss and smoothness of coated papers. In addition to the improvements in surface characteristics, calendering decreases coating pore volume and pore size, by permanently compressing the coating layer. The surface pores, in particular, are affected, which might lead to reduced ink setting speed.

Kosse et al. [5] confirmed the reduction of pore volume during calendering and showed that this pore volume reduction of the whole paper can be up to 48% compared with uncalendered papers. The pore volume reduction primarily occurs in the base paper (fiber matrix), but the coating layer also becomes compressed and the typical pore diameter shifts to smaller diameters.

Larsson et al. [13] demonstrated that calendering of coated paper significantly reduces pore volume and pore size. They found that pore volume of pure clay coating is reduced twice as much as those of pure ground calcium carbonate (GCC) coating. Collapsing of the loose structure built by the platy clay particles during calendering can be limited by addition of 30% GCC. Calendering of coated papers leads to a denser surface structure with more aligned clay particles, as highlighted by Hiorns et al. [14]. Based on SEM results, the reduced ink setting behavior of calendered papers is a result of the lower pore volume of the coating layer and by a denser surface structure with a reduced number of pores per unit area. Both changes, the dense surface and the reduced pore volume, retard ink vehicle absorption of calendered papers, which was also noted by Bluvol et al. [15].

Elton et al. [16] analyzed the influence of nip passes on the roughness of coated papers by use of polarized light reflectometry and found that the first few nip passes decrease macroroughness, probably due to smoothing of the base paper. A larger number of nip passes led to a decrease of the refractive index and the microroughness.

The influence of viscoelastic behavior of paper coating on the end use performance of coated papers was studied by Kan et al. [17]. Higher gloss is realized with coating having lower elastic modulus (higher compressibility). The viscoelastic

properties of paper coating are determined by the viscoelasticity of the used latex and the volume fractions of the pigment, binder and voids. Coatings containing plastic pigments have comparatively higher uncalendered paper gloss (due to lower shrinkage) and higher glossability at calendering (due to higher void volume in the coating). An increase of latex content leads to a higher compressibility of the immobilized coating structure. This observation is explained by an improved lubrication of the pigments and the collapse of bridges between pigment particles under high temperature and high load [18]. The influence of latex on the deformation behavior of coating structure during calendering was investigated by Mikkila et al. [19]. When hard latex (high glass transition temperature Tg) is used, the high stiffness of the coating reduces the ability of the coating to deform. The soft latex (low Tg) restricts deformation during calendering due to film forming. Coatings containing the latex with intermediate Tg can be deformed most easily. Furthermore, calendering at low temperature influences the porosity of the coating more than the gloss of the coating layer.

Information in the literature is based on investigations of different paper grades. For our investigations we linked pore structure and the surface porosity of wood-free multiply coated calendered papers with ink setting. We also wanted to determine whether the current penetration models describing the ink solvent absorption into coating structures are valid for describing the influence of induced pore changes by calendering on the ink setting behavior of the final calendered paper.

MATERIALS AND METHODS

For our experiments we used a commercial wood-free triple-coated paper with a grammage of 135 g/m². We used 100% coarse GCC for the precoating and middle coating and a blend of 80% fine GCC and 20% clay for the top coating.

We used a Kleinwefers laboratory calender (a two-roll system consisting of a heated steel roll and a soft wool paper roll) to investigate the influence of steel roll temperature, number of calender passes, and line load. The experiments consisted of three parts:

- Series 1: Varied steel roll temperature (25°C, 50°C, 70°C and 90°C) at constant number of passes (10 passes) and constant line load (30 N/mm).
- Series 2: Varied number of passes (two, four, six, and 10 passes) at constant steel roll temperature (70°C) and constant line load (30 N/mm).
- Series 3: Increased line load (30 and 120 N/mm) at constant number of passes (10 passes) and constant steel roll temperature (70°C).

nip passes calender temperature line load		uncalendered	2 passes 25°C 30 N/mm	4 passes 25 °C 30 N/mm	6 passes 25°C 30 N/mm	10 passes 25 °C 30 N/mm	2 passes 50°C 30 N/mm	4 passes 50°C 30 N/mm	6 passes 50 °C 30 N/mm	10 passes 50°C 30 N/mm
grammage	g/m≤	135	135	135	135	135	135	135	135	135
specific volume	cm≥/g	0,83	0,77	0,75	0,76	0,75	0,74	0,72	0,72	0,73
caliper	mm	0,112	0,104	0,102	0,102	0,102	0,1	0,098	0,098	0,098
paper gloss Tappi 75 ° top side	%	54	64	68	69	73	70	73	74	76
paper gloss Tappi 75 ° wire side	%	52	66	69	72	74	71	74	76	78
paper gloss DIN 75° top side	%	24	36	42	45	49	47	52	55	60
paper gloss DIN 75° wire side	%	20	32	37	41	45	44	51	55	56
paper gloss DIN 45° top side	%	4	7	9	11	14	10	13	17	20
paper gloss DIN 45° wire side	%	3	6	8	9	12	10	13	15	18
mean Tappi 75°	%	53	65	68	71	74	71	74	75	77
mean DIN 75°	%	22	34	40	43	47	46	52	55	58
mean DIN 45°	%	3	7	8	10	13	10	13	16	19
roughness PPS top side	µm	1,5	1,0	0,9	0,8	0,8	0,8	0,7	0,7	0,6
roughness PPS wire side	µm	1,8	1,2	1,1	1,0	0,9	0,9	0,8	0,8	0,7
Set-off 15s top side		0,78				0,96				0,99
Set-off 30s top side		0,44				0,66				0,76
Set-off 60s top side		0,15				0,24				0,28
Set-off 120s top side		0,04				0,03				0,03

I. Analyzed paper properties of uncalendered paper and papers calendered at 25°C and 50°C.

nip passes calender temperature line load		uncalendered	2 passes 70°C 30 N/mm	4 passes 70°C 30 N/mm	6 passes 70°C 30 N/mm	10 passes 70°C 30 N/mm	2 passes 70°C 120 N/mm	4 passes 70°C 120 N/mm	6 passes 70°C 120 N/mm	10 passes 70°C 120 N/mm
grammage	g/m≤	135	135	135	135	135	135	135	135	135
specific volume	cm≥/g	0,83	0,72	0,70	0,70	0,69	0,68	0,68	0,68	0,67
caliper	mm	0,112	0,097	0,095	0,094	0,093	0,092	0,091	0,091	0,090
paper gloss Tappi 75° top side	%	54	74	77	79	80	83	85	86	87
paper gloss Tappi 75° wire side	%	52	77	78	79	81	84	86	87	88
paper gloss DIN 75° top side	%	24	61	65	66	69	72	76	78	78
paper gloss DIN 75° wire side	%	20	60	67	69	71	72	77	78	81
paper gloss DIN 45° top side	%	4	17	22	24	27	31	38	42	44
paper gloss DIN 45° wire side	%	3	20	24	26	30	33	41	44	47
mean Tappi 75°	%	53	75	78	79	80	83	85	86	87
mean DIN 75°	%	22	61	66	67	70	72	76	78	79
mean DIN 45°	%	3	18	23	25	29	32	39	43	45
roughness PPS top side	µm	1,5	0,6	0,6	0,5	0,5	0,6	0,5	0,5	0,5
roughness PPS wire side	µm	1,8	0,7	0,6	0,5	0,5	0,6	0,5	0,5	0,4
Set-off 15s top side		0,78	1,04	1,05	1,04	1,03				1,02
Set-off 30s top side		0,44	0,82	0,86	0,83	0,84				0,72
Set-off 60s top side		0,15	0,35	0,35	0,33	0,37				0,33
Set-off 120s top side		0,04	0,04	0,04	0,04	0,04				0,03

II. Analyzed paper properties of uncalendered paper and papers calendered at 70°C with different line load.

The following standard properties of uncalendered and calendered papers were analyzed:

- **grammage [g/m²]** (ISO 536),
- **caliper [µm]** (ISO 534),
- **specific volume [cm³/g]** (ISO 534),
- **paper gloss TAPPI 75° [%]** (TAPPI T480),
- **paper gloss DIN 75° [%]** (DIN 54502),
- **paper gloss DIN 45° [%]** (DIN 54502),
- **PPS roughness [µm]** (ISO 8791-4), and
- **set-off** (measured 15, 30, 60, and 120 seconds after printing; Zellcheming reference sheet "Test of the ink setting behavior of ink and paper," 1999).

We used a mercury porosimeter to characterize the pore structure of the test papers (uncalendered and calendered). Pore structure data were corrected using the Pore-comp software (University of Plymouth, UK). The surface porosity was analyzed by image analysis on a series of SEM images. **Tables I-III** show detailed results of the investigations.

RESULTS AND DISCUSSION

The mercury porosimetry results (**Figs. 3-5**) confirm that the fiber network of the base paper is permanently compressed during calendering. A stepwise decrease of characteristic pore diameter and void volume (porosity) is found with increased steel roll temperature (Fig. 3). The influence of calender settings also is visible in the pore diameter range typical for the coating layer, but it is not as pronounced as for the fiber network. When the number of passes is changed at constant temperature, the final effect on pore structure is already reached after four passes through the laboratory calender (Fig. 4); a further increase in the number of nips does not result in any significant further change in the pore structure. An increase of nip load from 30 to 120 N/mm results in a significantly higher compression of the whole paper structure as presented in Fig. 5.

Figure 6 shows the well-known trend that paper gloss increases with raising calendering temperature at con-

nip passes calender temperature line load		uncalendered	2 passes 90°C 30 N/mm	4 passes 90°C 30 N/mm	6 passes 90°C 30 N/mm	10 passes 90°C 30 N/mm
grammage	g/m≤	135	135	135	135	135
specific volume	cm∃g	0,83	0,70	0,69	0,69	0,69
caliper	mm	0,112	0,094	0,093	0,092	0,092
paper gloss Tappi 75° top side	%	54	77	80	81	81
paper gloss Tappi 75° wire side	%	52	81	84	84	84
paper gloss DIN 75° top side	%	24	68	73	73	74
paper gloss DIN 75° wire side	%	20	71	76	78	78
paper gloss DIN 45° top side	%	4	23	29	31	31
paper gloss DIN 45° wire side	%	3	29	37	38	39
mean Tappi 75°	%	53	79	82	82	83
mean DIN 75°	%	22	69	75	75	76
mean DIN 45°	%	3	26	33	34	35
roughness PPS top side	µm	1,5	0,5	0,4	0,4	0,4
roughness PPS wire side	µm	1,8	0,6	0,4	0,4	0,4
Set-off 15s top side		0,78				1,04
Set-off 30s top side		0,44				0,85
Set-off 60s top side		0,15				0,40
Set-off 120s top side		0,04				0,06

III. Analyzed paper properties of uncalendered paper and papers calendered at 90°C.

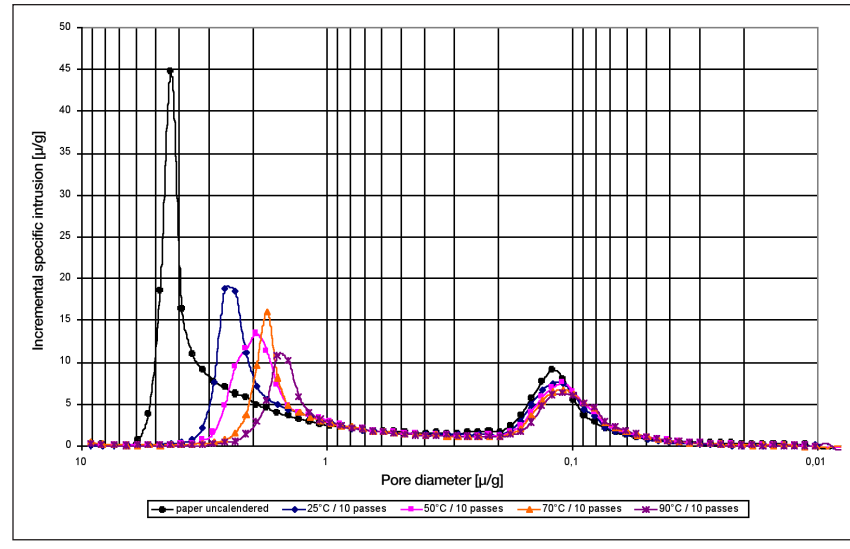

3. Series 1: The influence of calendering temperature on pore structure (mercury porosimetry).

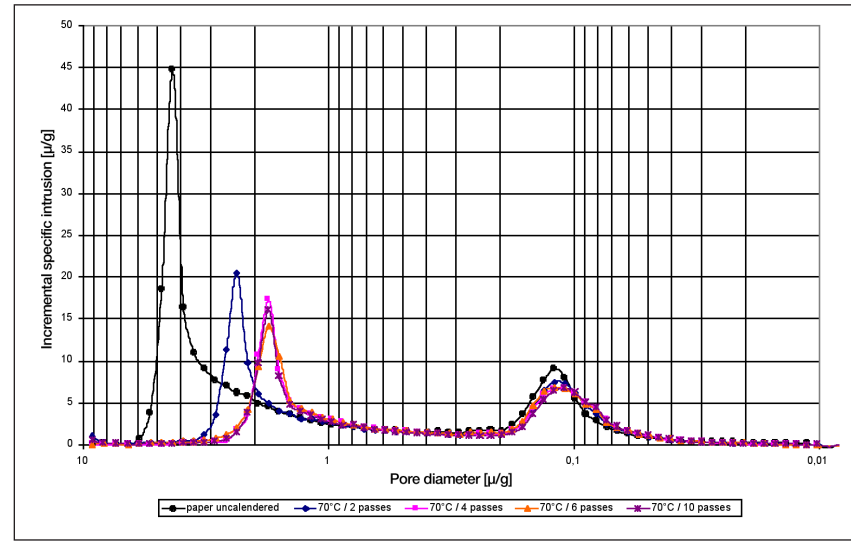

4. Series 2: The influence of the number of nip passes on pore structure (mercury porosimetry).

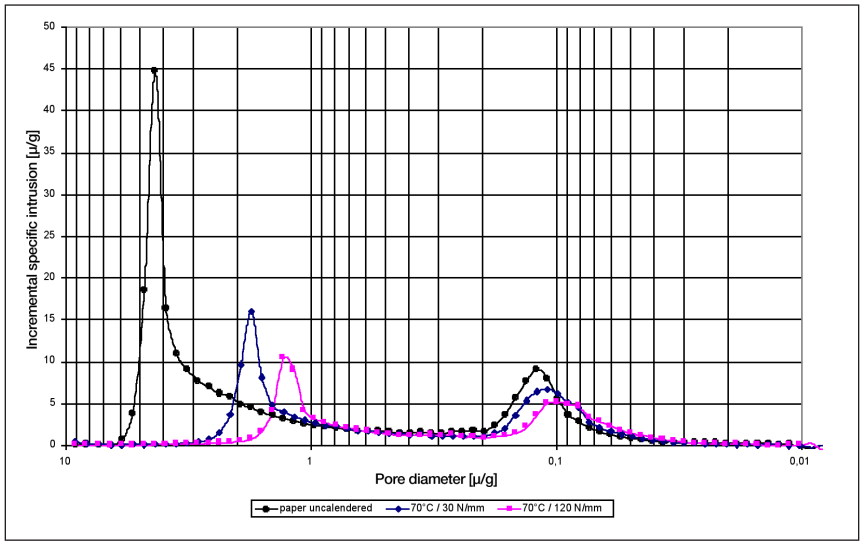

5. Series 3: The influence of nip load on pore structure (mercury porosimetry).

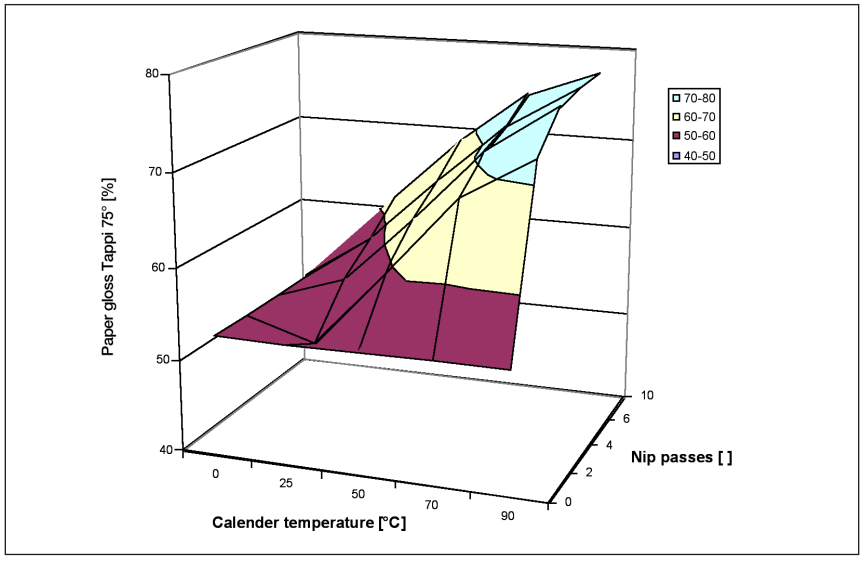

6. Paper gloss TAPPI 75° as a function of calendering temperature and nip passes (mean of top and wire side).

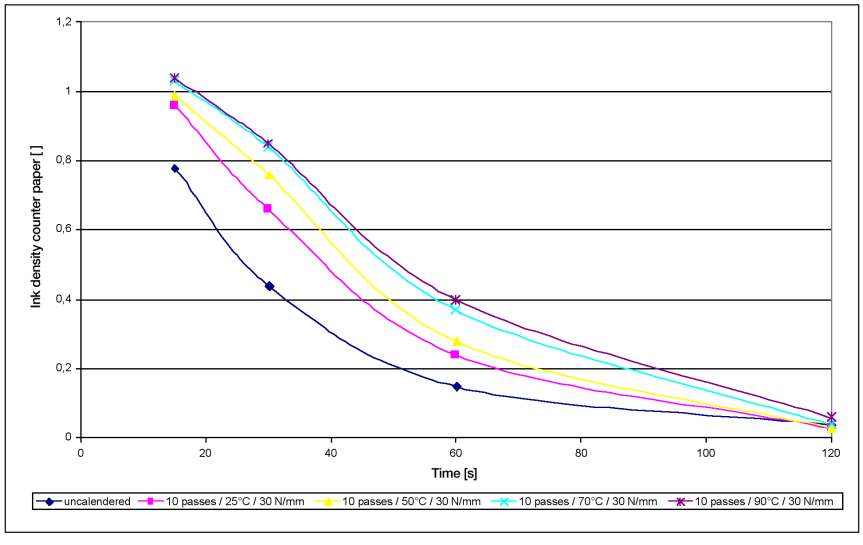

7. Ink density on counter paper as a function of steel roll temperature at calendering.

stant number of passes, as well as with increased number of passes at constant calendering temperature. The influence of calendering temperature on paper gloss is higher than the influence of the number of passes. For highest gloss levels, high calendering temperature is essential.

The ink setting behavior of the papers was tested with the set-off test, according to Zellcheming guidelines. On the Prüfbau printing tester we used, a defined ink film is applied and the printed paper is countered against a blank piece of paper after defined time intervals. The faster the ink setting of the paper, the lower is the ink density measured on the counter paper.

Figure 7 shows that ink setting rate is slower when steel roll temperature is increased. An increase in the number of passes through the laboratory calender from two to 10 at constant steel roll temperature showed no significant effect on ink setting rate (**Fig. 8**). Calendering temperature dominates the change of pore structure; the number of passes had no significant influence.

Surface pore size was determined on five SEM images per paper sample (total area evaluated per SEM image was 90 µm²) acquired at a resolution of 0.01 µm per pixel (Fig. 1). A grey level threshold was set manually on each image and all closed image regions darker than the threshold were considered as pores. With this analysis of the SEM images the following surface structure descriptive data were obtained:

- pore size of each pore,
- perimeter of each pore,
- pore area of each pore,
- total pore area (sum of all pore areas detected),
- hydraulic diameter of each pore (equivalent to 4 * pore area over pore perimeter),
- median pore diameter (hydraulic) – 50% of the pores have a pore size smaller than the median pore diameter, and
- number of surface pores detected.

As shown in **Table IV**, the median pore diameter (calculated from the hy-

draulic diameter) decreased with increasing steel roll temperature. The total area of the surface pores decreases with increasing temperature of the steel roll temperature, with the exception of the paper calendered at 70°C. Reduction of the surface porosity also can be observed in the SEM images (Fig. 1).

When the absolute values of the analyzed pore size data are compared, the typical pore size of the surface pores detected with image analysis of the SEM images is significantly smaller than pore size values from mercury porosimetry. The surface pores are smaller than the average pore structure of the whole coating layer, but method-related deviations cannot be ruled out [20].

Image analysis gives a distribution of pore size by number of pores, whereas mercury porosimetry gives a distribution of size by volume. For a given pore volume, a larger number of small pores or fewer large ones are possible. A number distribution might therefore be expected to be shifted to a smaller pore size compared with a volume distribution. However, this attempt to analyze the pore structure of the coating layer with image analysis needs further optimization. A higher number of analyzed areas per sample likely would improve the statistical variability.

Results from our investigation demonstrate that the average pore size of coated papers is permanently compressed and reduced by calendering. According to theory, small pore sizes should speed up ink setting. This effect is compensated by closing of the surface pores. Reduction of surface porosity ε dominates and leads to an actually slower ink setting for calendered papers. Closing of the surface pores can be explained by the increased film forming propensity of the latex and the forced alignment of the coating layer's pigments during calendering.

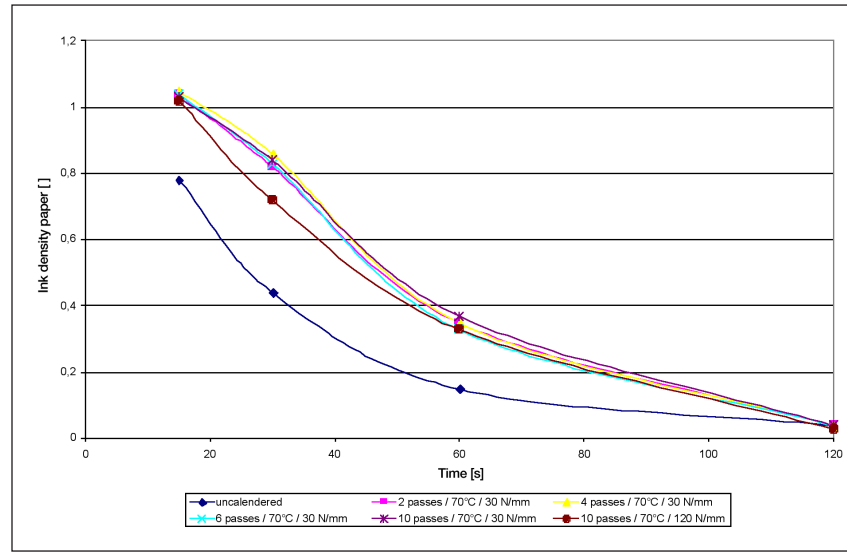

8. Ink density on counter paper as a function a function of the number of passes through calender.

Coating concepts that enable us to reach the desired paper gloss by the right choice of pigments without calendering are advantageous when fast ink setting is a priority. If calendering is required to reach a targeted gloss level, we propose calendering at comparatively lower roll temperature and a higher number of nip passes. Still, for high gloss papers, high calendering temperature will be necessary to reach the required gloss level (i.e., compare Fig. 7 and Fig. 8).

CONCLUSIONS

Fast ink setting in offset coated papers can be realized using fine pigments and pigments with a steep particle size distribution. Ink-paper interaction of coated papers is, however, significantly influenced by calendering. The pore size of coated papers is permanently reduced by compression during calendering. Mercury porosimetry and image analysis of SEM images showed a reduction of total pore volume, in combination with reduced surface porosity. Small pores theoretically should improve ink setting, but the closing of surface pores dominates and actually results in slower ink setting for calendered papers. This can be explained by a denser coating surface, which is a result of latex melt flow under high temperatures, when temperature exceeds latex Tg and as the forced alignment of the coating layer. For clay-containing coatings, higher closing of the surface porosity due to the alignment of platey clay particles is expected at calendering. **TJ**

ACKNOWLEDGEMENT

I am grateful to my colleagues in the Sappi Europe R&D Department for their support in this work, and thank Sappi Fine Paper Europe for permission to publish this work.

	Uncalendered	10 passes 25°C 30 N/mm	10 passes 50°C 30 N/mm	10 passes 70°C 30 N/mm	10 passes 90°C 30 N/mm
Number of surface pores [ ]	444	495	328	507	339
Median pore diameter [µm]	0.099	0.086	0.084	0.083	0.072
Total pore area [µm²]	4.45	3.60	2.48	3.30	1.72

IV. Results of image analysis of SEM images (description of the used calendering setting: nip passes / steel roll temperature / nip load).

LITERATURE CITED

1. FOGRA, *Annual Report 2006*, Fogra Forschungsgesellschaft Druck e.V., Munich, Germany, 2007.
2. Resch, P., "Pore structure analysis of coated papers by use of mercury porosimetry and the influence of pore structure on printability," Diploma thesis, Graz University of Technology, Austria, 2001.
3. Resch, P., and Bauer, W., *Proceedings of the 23rd PTS Coating Conference*, Papiertechnische Stiftung, Munich, Germany, 2007, pp. 12.1-15.
4. Nutbeem, C., Husband, J.C., and Preston, J.S., *Proceedings of the PITA Coating Conference*, Paper Industry Technical Association, Bury, United Kingdom, 2005, pp. 97-102.
5. Kosse, J., Kleemann, S., Naydowski, C., et al., *Wochenbl. f. Papierf.* 131(7): 348(2003).
6. Donigian, D., "The coating-ink interface and the setting of offset printing ink," *Proceedings of PTS Seminar: Interface Chemistry, PTS*, Papiertechnische Stiftung, Munich, 2005.
7. Schölkopf, J., "Observation and modelling of fluid transport into porous paper coating structures," Ph.D. thesis, University of Plymouth, England, 2002.
8. Schölkopf, J., Gane, P., and Ridgway, C., *Nordic Pulp Paper Res. J.* 15(5): 422(2000).
9. Preston, J., "The influence of coating structure on the print gloss of coated paper surfaces," Ph.D. thesis, University of Bristol, England, 2001.
10. Preston, J., Elton, N., Legrix, A., et al., *TAPPI J.* 1(3): 3(2002).
11. Xiang, Y., and Bousfield, D., *J. Pulp Paper Sci.* 26(6): 221(2000).
12. Xiang, Y., Bousfield, D., Hayes, P., et al., *J. Pulp Paper Sci.* 30(5): 117(2004).
13. Larsson, M., Vidal, D., Engström, G., et al., *Proceedings of the 22nd PTS Coating Symposium*, Papiertechnische Stiftung, Munich, 2005, pp. 24.1-16.
14. Hiorns, A., Elton, J., Coggan, L., et al., *Proceedings of the 1998 TAPPI Coating and Papermakers Conference*, TAPPI PRESS, Atlanta, Georgia, USA, pp. 583-602.
15. Bluvol, G., Burri, P., Carlsson, R., et al., *Proceedings of the 21st PTS Coating Symposium*, Papiertechnische Stiftung, Munich, 2003, pp. 17.1-17.
16. Elton, N.J., and Preston, J.S., *TAPPI J.* 5(8): 10(2006).
17. Kan, C., Kim, L., Lee, D., et al., *TAPPI J.* 80(5): 191(1997).
18. Larsson, M., Engström, G., Vidal, D., et al., "Compression of coating structure during calendering," *Proceedings of the 9th TAPPI Advanced Coating Fundamentals Symposium*, TAPPI PRESS, Atlanta, 2006.
19. Mikkilä, J., Jarvinen, H., Starck, P., et al., Wochenbl. *f. Papierf.* 130(20): 1328(2002).
20. Vyörykkä, J., Fogden, A., Daicic, J., et al., "Characterization of paper coatings – review and future possibilities," *Proceedings of 9th TAPPI Advanced Coating Fundamentals Symposium*, TAPPI PRESS, Atlanta, 2006.

INSIGHTS FROM THE AUTHORS

The starting point of my Ph.D. work (dealing with physical and chemical ink drying mechanisms) was the study of currently available models describing the effect of pore structure on ink setting behavior. With this study I tried to find similarities between the most common penetration models. I also checked whether these common models are able to describe changes resulting from calendering.

The most difficult aspect of this research was determining surface porosity. This was addressed by using image analysis tools developed at the University of Technology in Graz (Institute for Paper, Pulp and Fibre Technology).

One of the most interesting findings from this study is that the common models also can be used to describe the effect of pore structure changes due to calendering on ink setting behavior of triple-coated papers.

This work highlights basics for the optimization of calendering parameters to reach a balance for paper gloss and ink setting.

Resch

Bauer

Hirn

Resch is with Sappi Austria Produktions GmbH & Co. KG, Gratkorn, Austria; Bauer and Hirn are with Graz University of Technology, Institute for Paper, Pulp and Fibre Technology, Graz, Austria. E-mail Resch at peter.resch@sappi.com.